ACCSCIENCE PUBLISHING

International Journal of Bioprinting

RESEARCH ARTICLE

A vascularized 3D-bioprinted model of the osteosarcoma microenvironment reveals a proliferation-to-invasion switch that confers chemoresistance

Guang Tang[1,2†], Zhongte Peng[3†], Ying Zhao[4†], Xin Chen[4], Shuai Huang[5*], Guangfu Chen[6*], and Wei Guo[4*]

[1]Department of Orthopedics, First Affiliated Hospital of Jinan University, Guangzhou, Guangdong, China

[2]Department of Spinal Surgery, the Affiliated Hospital of Xiangnan University, Chenzhou, Hunan, China

[3]Institute of Precision Medicine, The First Affiliated Hospital of Sun Yat-sen University, Guangzhou, Guangdong, China

[4]Department of Orthopedic Surgery, The First Affiliated Hospital, Sun Yat-Sen University, Guangzhou, Guangdong, China

[5]Department of Orthopaedic Surgery, The First People's Hospital of Foshan, School of Medicine, Southern University of Science and Technology, Foshan, Guangdong, China

[6]Department of Spinal Surgery, Foshan Fosun Chancheng Hospital, Foshan, Guangdong, China

[†]*These authors contributed equally to this work.*

***Corresponding authors:**
Shuai Huang
(huangshuai316@163.com)
Guangfu Chen
(13553328753@163.com)
Wei Guo
(guowei27@mail.sysu.edu.cn)

Citation: Tang G, Peng Z, Zhao Y, *et al*. A vascularized 3D-bioprinted model of the osteosarcoma microenvironment reveals a proliferation-to-invasion switch that confers chemoresistance. *Int J Bioprint.* 2026:12(2):026040031. doi: 10.36922/IJB026040031

Received: January 25, 2026

Revised: March 31, 2026

Accepted: April 7, 2026

Published online: April 24, 2026

Abstract

The tumor microenvironment (TME) is a major driver of osteosarcoma progression, metastasis, and therapeutic resistance, yet conventional models fail to effectively recapitulate the multicellular interactions and biomechanical cues of the bone niche. In this study, we developed a vascularized 3D-bioprinted osteosarcoma model using a biomimetic hydrogel composed of decellularized extracellular matrix, chondroitin sulfate, and hydroxyapatite. U2OS osteosarcoma cells, human mesenchymal stem cells (HMSCs), and human umbilical vein endothelial cells were co-cultured within the printed constructs. Confocal imaging, RNA sequencing, xenograft validation, and integration with clinical single-cell RNA-sequencing data were used to define TME-driven changes in tumor behavior. The engineered TME induced a proliferation-to-invasion switch characterized by G0/G1 arrest, reduced proliferation activity, and enhanced invasiveness, angiogenic potential, and extracellular-matrix remodeling. Transcriptomic profiling showed downregulation of cell-cycle programs, including E2F and MYC targets, together with activation of TGF-β signaling, epithelial–mesenchymal transition (EMT), and hypoxia-related pathways. Mechanistically, HMSCs were identified as key regulatory cells that promoted migratory programs in tumor cells, partly through CXCL chemokine signaling engaging CXCR2. The TME-induced state also conferred robust chemoresistance to paclitaxel, associated with cell-cycle quiescence and pro-survival signaling, such as NF-κB activation. Critically, the transcriptional signature of these quiescent-invasive cells closely mirrored that of a clinically observed osteosarcoma subpopulation with low proliferation and high EMT activity. This high-fidelity vascularized 3D-bioprinted model recapitulates major TME-dependent features of osteosarcoma and provides a biologically

relevant platform for studying tumor plasticity and evaluating therapies targeting microenvironment-driven treatment resistance.

Keywords: Osteosarcoma; Tumor microenvironment; 3D bioprinting; Chemoresistance; Mesenchymal stem cells; Phenotypic switching

1. Introduction

Osteosarcoma, the most common primary malignant bone tumor, predominantly affects children, adolescents, and young adults, with a slightly higher incidence in males.[1] Although advances in surgery and neoadjuvant chemotherapy have improved the 5-year survival rate of patients with localized disease to approximately 60–70%[1], the prognosis of patients with metastatic osteosarcoma remains poor, with survival rates still below 30%.[1] As the lungs are the most common site of metastasis[2], this persistent survival gap highlights the need to better understand the biological mechanisms that drive osteosarcoma progression, dissemination, and treatment failure.

Accumulating evidence indicates that these processes are strongly shaped by the tumor microenvironment (TME).[3] The osteosarcoma TME is a heterogeneous and dynamic ecosystem composed of tumor cells, stromal cells, immune cells, endothelial cells (ECs), and extracellular matrix (ECM) components.[4] Together, these elements provide biochemical and biomechanical cues that influence tumor cell proliferation, invasion, angiogenesis, and therapeutic response.[4,5] Thus, the TME is increasingly recognized not simply as a structural scaffold, but as an active regulator of osteosarcoma behavior.[6]

Despite this, *in vitro* osteosarcoma research has long relied primarily on two-dimensional (2D) culture systems, in which cells grow as monolayers on rigid plastic surfaces. These models are easy to use, but they poorly reproduce three-dimensional (3D) tissue architecture, cell–cell and cell–ECM interactions, and gradients of oxygen, nutrients, and drug penetration.[6] Animal models provide additional physiological relevance, yet are limited by cost, ethical concerns, low throughput, and interspecies differences.[7] Together, these limitations create a persistent predictive gap in preclinical osteosarcoma research, particularly for TME-dependent phenotypes such as invasion, plasticity, and chemoresistance.[8]

To address these shortcomings, 3D *in vitro* models have emerged as promising tools for osteosarcoma research.[9] Current 3D osteosarcoma models can be broadly divided into scaffold-free systems, such as multicellular spheroids, and scaffold-based systems, including synthetic polymer scaffolds, natural hydrogels, and hybrid biomaterial platforms.[10] Scaffold-free models can reproduce basic cell–cell interactions and spatial heterogeneity, but they do not adequately capture the matrix support, mineralized context, or structural complexity of the native bone niche.[10] Scaffold-based systems provide improved 3D support, yet still have important limitations. Synthetic materials such as polycaprolactone or poly(lactic-co-glycolic acid) offer mechanical stability but often lack intrinsic bioactivity[11], whereas single-component natural hydrogels are generally more cytocompatible but fail to reproduce the mineralized and biochemical complexity of osteosarcoma in bone.[4]

This limitation is particularly important in osteosarcoma, where tumor behavior is shaped not only by 3D structure, but also by the bone-like niche itself. Osteosarcoma develops in a microenvironment characterized by mineralized matrix cues, marrow-associated stromal support, vascular interactions, and active paracrine signaling. However, most reported 3D models capture only one or two of these features and rarely integrate mineralized matrix properties, stromal heterogeneity, and vascular organization within a single controllable platform.[12] As a result, many existing systems remain insufficient for studying how the TME influences osteosarcoma phenotypic plasticity and treatment response.[13] This issue is especially relevant given the context-dependent roles of stromal cells such as mesenchymal stem cells (MSCs) and the increasingly recognized contribution of the TME to chemoresistance.[14]

Three-dimensional bioprinting offers a promising strategy to address these challenges.[15] By enabling precise spatial control over multiple cell types and materials, 3D bioprinting allows the construction of more biomimetic and experimentally tractable tumor models.[16] In particular, its ability to pattern multicellular architectures makes it well suited for reconstructing stromal–tumor–vascular interactions that are difficult to model in conventional systems.[17]

In this study, we developed a vascularized 3D-bioprinted osteosarcoma microenvironment model based on a composite hydrogel composed of decellularized

extracellular matrix (dECM), chondroitin sulfate (CS), and hydroxyapatite (HAP).[18] This biomaterial design was intended to approximate both the soft stromal characteristics of bone marrow and the mineralized properties of the osteosarcoma niche.[19] At the same time, multi-nozzle 3D bioprinting enabled the controlled tri-culture of osteosarcoma cells, human mesenchymal stem cells (HMSCs), and human umbilical vein endothelial cells (HUVECs), thereby incorporating stromal and vascular components into the same engineered construct.[20]

Using this model, we sought to determine whether a multicellular, vascularized, and bone-mimetic microenvironment is associated with changes in osteosarcoma cell state, particularly with respect to proliferation, invasion-associated features, and chemosensitivity.[21] By integrating phenotypic analyses, transcriptomic profiling, comparison with public clinical single-cell data, and *in vivo* validation, we aimed to establish a more biologically relevant platform for investigating osteosarcoma microenvironmental biology and for evaluating therapeutic strategies targeting TME-associated tumor plasticity.[22]

2. Methods

All key commercial reagents, kits, and antibodies used in this study are summarized in Table 1.

2.1. Cell lines, culture conditions, and quality control

This study utilized four human cell lines: osteosarcoma cells U2OS and 143B, primary HMSCs, and HUVECs. To ensure the reliability and reproducibility of experimental data, all cell lines were authenticated via short tandem repeat profiling and routinely tested for mycoplasma contamination using polymerase chain reaction (PCR)-based assays.

All cells were cultured in a humidified incubator at 37 °C with 5% CO_2. The 143B cells were maintained in high-glucose Dulbecco's Modified Eagle Medium supplemented

Table 1. Main experimental reagents and antibodies

Cell line/Reagent/Antibody	Supplier (Country)	Cat. No.
Human osteosarcoma cell lines (U2OS and 143B)	AoRuiCell Biology (China)	AoRuiCell
Human primary bone marrow mesenchymal stem cells	AoRuiCell Biology (China)	AoRuiCell
Human umbilical vein endothelial cell line	AoRuiCell Biology (China)	AoRuiCell
High-glucose DMEM medium	Gibco (United States of America [USA])	C11995500BT
Mesenchymal stem cell-specific medium	AoRuiCell Biology (China)	AoRuiCell
Endothelial cell growth medium-2	Lonza (Switzerland)	CC-3156
Fetal bovine serum, Prime	Vazyme (China)	F103
Penicillin-Streptomycin solution	Gibco (USA)	15140122
0.25% Trypsin-EDTA	Gibco (USA)	25200072
Polybrene	Sigma-Aldrich (USA)	H9268
Puromycin	Sigma-Aldrich (USA)	P8833
Paclitaxel	Sigma-Aldrich (USA)	T7402
D-luciferin	Gold Biotechnology (USA)	LUCNA-1G
LIVE/DEAD™ Cell Cytotoxicity Assay Kit	Invitrogen (USA)	L3224
Cell Counting Kit-8	Dojindo (Japan)	CK04
Annexin V-FITC/PI Apoptosis Detection Kit	Vazyme (China)	A211-02
TRIzol™ Reagent	Invitrogen (USA)	15596026
Reverse Transcription Kit	Vazyme (China)	R323-01
SYBR Green Master Mix	Vazyme (China)	Q711-02
Anti-Ki-67 antibody (IHC)	Proteintech (China)	27308
Anti-CD31 antibody (IHC)	Proteintech (China)	11265
Anti-vimentin antibody (IHC)	Proteintech (China)	10366
Anti-α-SMA antibody (IHC)	Proteintech (China)	14395

with 10% fetal bovine serum (FBS) and 1% penicillin–streptomycin. U2OS and HMSCs were cultured in MSC-optimized growth medium containing 10% FBS and 1% penicillin–streptomycin. HUVECs were cultured in EC growth medium-2, which includes 2% FBS and multiple critical growth factors (e.g., vascular endothelial growth factor) essential for maintaining the endothelial phenotype and promoting angiogenic function. The culture medium was replaced every 2–3 days. Cells were passaged using 0.25% trypsin-EDTA solution when confluence reached 80–90%.

2.2. Construction of stable reporter cell lines

To enable lineage tracing and analysis of specific cell populations, stable reporter-expressing cell lines were generated using lentiviral transduction in this study. U2OS, HMSC, and HUVEC cells were transduced to stably express mCherry (U2OS-mCherry), green fluorescent protein (HMSC-GFP), or mCherry (HUVEC-mCherry) or enhanced blue fluorescent protein (HUVEC-EBFP), respectively. For *in vivo* tumor formation experiments, 143B cells were transduced to stably express firefly luciferase (143B-LUC), allowing non-invasive, longitudinal monitoring of tumor growth via bioluminescence imaging.

The transduction protocol was as follows: cells were seeded in 6-well plates and allowed to adhere before being incubated with culture medium containing an appropriate titer of lentiviral particles and a final concentration of 8 μg/mL polybrene. After 72 h of transduction, the medium was replaced with fresh medium supplemented with puromycin at the optimal selection concentration (2 μg/mL). This concentration was determined based on a prior dose–response curve (kill curve) assay, defined as the lowest concentration capable of effectively killing 100% of non-transduced control cells. Cells were subjected to selection for at least one week until all control cells had died, thereby obtaining a purified population of stable transductants. U2OS cells stably expressing mCherry were used in the paclitaxel experiments, whereas U2OS-BFP cells were used in the cisplatin and doxorubicin validation experiments.

2.3. Preparation and characterization of hydrogel bioinks

2.3.1. Decellularized extracellular matrix preparation

The preparation of dECM followed a standardized multi-step decellularization protocol. In brief, fresh porcine dermal tissue was obtained, and the epidermis and adipose layers were removed mechanically before cutting the tissue into small fragments. The tissue fragments were then subjected to agitation in a solution containing 1% Triton X-100 and 0.25% EDTA at room temperature for 12–16 h to effectively remove cellular components.

Subsequently, the decellularized tissue was subjected to limited digestion with pepsin under acidic conditions (pH 2.0), converting the insoluble ECM network into a soluble precursor solution. Finally, the solution was dialyzed over a period of 7 days and then lyophilized to obtain purified dECM powder. Prior to use, the dECM powder was resuspended in hydrochloric acid solution (pH 3.5) to prepare a stock solution at a concentration of 15 mg/mL.

2.3.2. Formulation and physicochemical characterization of composite hydrogels

The final bioink selected for this study was a composite hydrogel based on dECM, nano-hydroxyapatite (nano-HAP), and CS. The final formulation consisted of 5–10 mg/mL dECM, 5 mg/mL CS, and 1% (w/v) nano-HAP.The physicochemical characterization analyses included:

(i) Microstructural analysis: The microstructure of the hydrogel was evaluated using scanning electron microscopy (SEM; Sigma 300, ZEISS, Germany). Freeze-dried hydrogel samples were sputter-coated with platinum prior to imaging, allowing assessment of internal pore architecture, pore size distribution, and dispersion of HAP particles.

(ii) Reflectance confocal imaging of hydrated type I collagen hydrogels: The fibrillar microstructure of type I collagen hydrogels was characterized by label-free reflectance confocal microscopy using an Olympus FV3000 laser scanning confocal microscope (Japan). To preserve the native hydrated architecture, the hydrogels were imaged directly under fully hydrated conditions without freeze-drying or dehydration. For imaging, a 488 nm laser was used for excitation, and the reflected signals were collected through the reflectance optical pathway within the 480–500 nm detection window. Representative images were acquired using either the transmitted detector (for transmitted-light/differential interference contrast imaging) or the high-sensitivity spectral detector (for high-sensitivity fluorescence detection). The pinhole was set to 1 Airy unit (1 AU). Laser power, detector sensitivity, and related acquisition settings were adjusted empirically to maintain sufficient signal intensity while avoiding signal saturation. For 3D visualization of the collagen network, serial optical sections were acquired along the z-axis over a total depth of 80 μm, followed by maximum intensity projection of the z-stack. This method enabled direct visualization of the hydrated collagen fibrillar architecture, in which filamentous collagen fibers formed an interconnected network

containing abundant pore-like interfibrillar spaces.

(iii) Rheological and mechanical characterization: Rheological measurements were performed using a rotational rheometer (Physica MCR301, Anton Paar, Austria). Shear-thinning behavior was assessed via steady shear sweeps across a shear rate range of 0.1–100 s^{-1} at 15 °C. Dynamic frequency sweeps were conducted to evaluate the storage modulus (G′) and loss modulus (G″) of the crosslinked hydrogels. Additionally, mechanical stiffness was quantified using a Piuma nanoindenter (Optics11 Life, Netherlands) equipped with a probe of 25.5 μm radius. Young's modulus maps were acquired over a 500 × 500 μm^2 area in phosphate-buffered saline (PBS), to verify whether the hydrogel could recapitulate the mechanical properties of native osteosarcoma tissue.

(iv) Swelling and degradation properties: The swelling behavior of freeze-dried hydrogels was evaluated gravimetrically in PBS at 37 °C. For *in vitro* degradation studies, hydrogel samples were immersed in PBS containing physiologically relevant concentrations of collagenase and incubated at 37 °C for 14 days. Residual dry weights were measured periodically throughout the experiment. These assays were designed to confirm that the hydrogel exhibited structural stability and controllable degradation kinetics suitable for long-term cell culture.

2.4. 3D bioprinting of the osteosarcoma tumor microenvironment model

2.4.1. Printing system and strategy

All bioprinting procedures were performed within a sterile biosafety cabinet using a multi-nozzle micro-extrusion-based 3D bioprinter (SunP Biomaker 2, China). Cell-laden bioinks were prepared by gently mixing pre-cooled (4 °C) hydrogel solutions with cell suspensions on ice.

To systematically investigate the complexity of the TME, two bioprinting strategies were employed in this study:

(i) Tumor spheroid model (monoculture control): A single-nozzle printing approach was used to fabricate spherical structures with a diameter of 1 mm, consisting of bioink loaded with U2OS cells (or co-cultured with HMSCs).

(ii) Vascularized TME model (multicellular co-culture): A dual-nozzle bioprinting strategy was implemented. Nozzle 1 dispensed bioink containing U2OS and HMSCs to form the tumor micro-tissue at the center of the model, while Nozzle 2 delivered bioink loaded with HUVECs to generate a predefined vascular network surrounding the tumor micro-tissue.

2.4.2. Printing parameters and post-processing

Key printing parameters, including nozzle dimensions, platform temperature, printing speed, and extrusion rate, were carefully optimized and strictly controlled throughout the bioprinting process. Immediately after printing, the constructs were transferred to a 37 °C incubator and allowed to stabilize for 30 min. This step leveraged the thermoresponsive properties of the bioink to induce rapid gelation and secure structural integrity. Following gelation, the appropriate culture medium was added to support long-term cultivation of the printed constructs.

2.5. Cellular and pharmacological analyses

2.5.1. Cell viability, proliferation, and morphological analysis

On days 1, 3, 5, 7, and 14 of culture, the 3D constructs were stained with the LIVE/DEAD™ Cytotoxicity Assay Kit to assess cell viability. Confocal laser scanning microscopy (CLSM; Zeiss LSM, Germany, or FV3000, Olympus, Japan) was used for imaging. Fluorescent staining enabled the clear distinction between live (green) and dead (red) cells within the 3D structure.

To evaluate cytoskeletal morphology and spatial distribution, immunofluorescence imaging of F-actin (phalloidin staining) and nuclei (DAPI staining) was performed. High-resolution z-stack imaging using CLSM allowed for detailed 3D reconstruction of the internal architecture of the 3D constructs.

2.5.2. Cell recovery from 3D hydrogels and flow cytometric analysis

For quantitative analysis at the single-cell level, cells were first recovered from the hydrogel matrix. The hydrogels were incubated in PBS containing 1–3 mg/mL collagenase at 37 °C until complete degradation was achieved. Single-cell suspensions were then obtained by gentle pipetting.

The recovered cells were subjected to flow cytometric analysis (BD LSRFortessa, BD Biosciences, San Jose, CA, USA) for assessment of the cell cycle, apoptosis (Annexin V-FITC/PI), and live/dead status (Fixable Aqua Dye).

2.5.3. Drug dose–response and chemoresistance evaluation

Paclitaxel, a second-line chemotherapeutic agent for osteosarcoma, was selected for testing. The half-maximal inhibitory concentration (IC_{50}) of paclitaxel against

U2OS cells under 2D monoculture, 3D monoculture, and 3D co-culture (U2OS with HMSC) conditions was determined using the CCK-8 assay. For the 3D co-culture condition, the IC_{50} value was calculated based on the signal derived from U2OS cells after subtracting the contribution of HMSCs.

To further quantitatively evaluate TME-induced chemoresistance, a dual-validation strategy was employed:

(i) Imaging-based global assessment: Tumor spheroids (U2OS monoculture vs. U2OS/HMSC co-culture) exposed to 1 μM paclitaxel for 3 and 7 days were subjected to live/dead cell staining. Fluorescent signals were quantified using ImageJ software (version 1.53; https://imagej.net/ij/) to calculate the percentage of viable cells.

(ii) Flow cytometry-based specific assessment: To eliminate interference from HMSCs in the overall viability readout, the treated tumor spheroids were enzymatically dissociated into single-cell suspensions.

Subsequently, fluorescence-activated cell sorting (FACS) was employed to specifically isolate tumor cells based on the red fluorescent signal of U2OS-mCherry. Finally, Annexin V-FITC/PI apoptosis assay and live/dead staining were performed exclusively on the purified tumor cell population. This experimental design enables definitive confirmation that the observed chemoresistance is an intrinsic property conferred by the TME.

2.6. Molecular and systems biology analysis

2.6.1. Fluorescence-activated cell sorting and RNA extraction

For cell type-specific transcriptomic analysis, the vascularized TME constructs were enzymatically dissociated, and the three constituent cell types were individually sorted into collection tubes containing TRIzol using a multicolor flow cell sorter (BD FACSAria, BD Biosciences, San Jose, CA, USA), based on their intrinsic fluorescent reporter signatures (U2OS-mCherry, HUVEC-EBFP, HMSC-GFP).

2.6.2. Quantitative real-time polymerase chain reaction

Total RNA was extracted using TRIzol reagent. After evaluating the purity and concentration with NanoDrop (Thermo Fisher Scientific, Waltham, MA, USA), the RNA was reverse-transcribed into cDNA. The SYBR Green method was employed to perform gene expression analysis on a quantitative real-time PCR (RT-qPCR) instrument, with *GAPDH* serving as the internal reference gene. All primers were validated, and their sequences are listed in Table 2.

2.6.3. Bulk RNA sequencing and differential expression analysis

High-quality RNA extracted from sorted cells (TME co-culture group vs. 3D monoculture control group) was used for transcriptomic library preparation, followed by high-throughput sequencing on an Illumina NovaSeq platform (Illumina, San Diego, CA, USA)

The raw sequencing data were processed through the following bioinformatics pipeline: First, FastQC was employed for quality assessment. Adapter sequences and low-quality reads were then trimmed using tools such as Trimmomatic. Clean reads were aligned to the human reference genome using alignment software such as STAR. Gene-level read counts were generated using featureCounts or HTSeq-count.

In the R environment, the DESeq2 package was used to normalize the gene expression profiles and perform differential expression analysis. Differentially expressed genes (DEGs) were typically defined using thresholds

Table 2. Primer sequences for RT-qPCR of human genes

Gene symbol	Forward primer (5' → 3')	Reverse primer (5' → 3')
MMP9	GCCACTACTGTGCCTTTGAGTC	CCCTCAGAGAATCGCCAGTACT
MKI67	GGGCCAATCCTGTCGCTTAAT	GTTATGCGCTTGCGAACCT
PCNA	CCTGCTGGGATATTAGCTCCA	CAGCGGTAGGTGTCGAAGC
VEGFA	TTGCCTTGCTGCTCTACCTCCA	GATGGCAGTAGCTGCGCTGATA
CD34	CTACAACACCTAGTACCCTTGGA	GGTGAACACTGTGCTGATTACA
GAPDH	TGTGGGCATCAATGGATTTGG	ACACCATGTATTCCGGGTCAAT

of $|\log_2(\text{Fold Change})| > 1$ and adjusted p-value < 0.05. Results were visualized using volcano plots and heatmaps.

2.6.4. Pathway enrichment and gene set enrichment analysis

To understand the biological functional changes represented by DEGs at a systems level, pathway enrichment analysis was performed. Kyoto Encyclopedia of Genes and Genomes (KEGG) pathway enrichment analysis and gene set enrichment analysis (GSEA) were performed separately using the specified software and parameter settings, aiming to identify signaling pathways that were significantly regulated within the TME.

Furthermore, to capture broader trends in biological process alterations, GSEA was carried out on all expressed genes after ranking them based on their expression changes between the two groups. The analysis employed the "Hallmark" gene set collection from the Molecular Signatures Database.

2.6.5. Cell–cell communication network analysis

To investigate the mechanisms of multicellular interactions within the TME, transcriptomic data from each cell population were analyzed using the iTALK algorithm. iTALK leverages the ligand-receptor interaction database curated by CellPhoneDB to identify potential signaling communications between distinct cell types. By comparing the interaction networks of the TME group with those of the control group, the complexity of intercellular communication can be quantified, and key signaling axes can be identified.

2.6.6. Integration analysis of public single-cell RNA sequencing data

To validate whether the biological phenomena observed in the *in vitro* model are clinically relevant, this study downloaded and analyzed publicly available osteosarcoma single-cell RNA sequencing (scRNA-seq) datasets (GSE152048) from the Gene Expression Omnibus database.

The data analysis pipeline was primarily conducted using the Seurat package. Raw data were first loaded and subjected to quality control filtering, during which cells with more than 20% mitochondrial gene content were excluded. The data were then normalized using the SCTransform method. Principal component analysis was performed on the normalized dataset, and the k-nearest neighbors algorithm implemented in the FindNeighbors function was used to construct a similarity matrix. Clustering was carried out by adjusting the resolution parameter within the range of 0.3–1.0. Cell types were subsequently annotated manually based on canonical marker genes, identifying major cell populations such as tumor cells (*EPCAM*$^+$), MSCs (*NT5E*$^+$), and ECs (*CLDN5*$^+$).

To assess the clinical relevance of the *in vitro* TME model, gene expression signatures derived from the TME group were compared with tumor cell subpopulations identified in the clinical samples. Specifically, the AUCell R package was employed to calculate the activity scores of predefined gene sets within each clinical tumor subpopulation. By comparing these scores, it was found that the transcriptional signature of TME-induced tumor cells *in vitro* closely resembled a non-high-proliferative tumor subpopulation present in the clinical samples, thereby confirming the clinical fidelity of the *in vitro* model.

2.6.7. Bioinformatics analysis software

The bioinformatics analysis of transcriptomic and single-cell omics data was primarily performed within the R environment, using multiple publicly available software packages. These included Seurat (v4.1.0) for single-cell data analysis, DESeq2 (v1.36.0) for differential expression analysis, clusterProfiler (v4.4.4) for pathway enrichment analysis, AUCell (v1.18.0) for gene set activity scoring, iTALK (v0.1.0) for cell–cell communication analysis, and ggplot2 (v3.3.6) for data visualization.

2.7. *In vivo* animal experiments

2.7.1. Animal ethics, housing, and surgical implantation

All animal experiments were strictly conducted in accordance with the guidelines of the Institutional Animal Care and Use Committee at Guangzhou Huace Detection Co., Ltd., and were approved under ethical clearance number 202502002. A total of 12 our-week-old female BALB/c nude mice were used in this study and randomly assigned into two groups (n = 6 per group):

(i) Control group: Subcutaneous implantation of 3D-printed hydrogels containing only 143B-LUC cells.
(ii) TME group: Subcutaneous implantation of 3D-printed hydrogels containing three cell types (143B-LUC, HMSCs, and HUVECs).

Surgical procedures were performed under sterile conditions with isoflurane inhalation anesthesia.

2.7.2. Tumor growth monitoring and endpoint analysis

Tumor burden was non-invasively monitored using bioluminescence imaging on days 0, 7, 14, and 21 post-implantation. D-luciferin substrate (150 mg/kg) was

administered via intraperitoneal injection prior to imaging. Bioluminescence signals were captured using an IVIS Spectrum imaging system (PerkinElmer, Waltham, MA, USA).

At the experimental endpoint (day 21), mice were euthanized, and the tumors were excised for further analysis. Tumor volume was calculated using the formula:

$$V = (L \times W^2)/2 \quad (1)$$

where L represents length and W represents width. Tumor wet weight was also recorded.

2.7.3. Histological and immunohistochemical analysis

Excised tumor tissues were fixed in 4% neutral buffered formalin, paraffin-embedded, and sectioned into consecutive 5 μm-thick slices. Standard hematoxylin and eosin staining and Masson's Trichrome staining (Servicebio, China) were performed to evaluate tissue morphology and collagen deposition, respectively.

To further validate the findings observed *in vitro*, IHC staining was carried out. Following deparaffinization, rehydration, and heat-induced antigen retrieval using citrate buffer (pH 6.0), endogenous peroxidase activity was blocked with 3% H_2O_2. Sections were then incubated with normal goat serum for blocking.

Subsequently, tissue sections were incubated overnight at 4 °C with primary antibodies specific to the target proteins. The next day, sections were incubated with horseradish peroxidase (HRP)-conjugated secondary antibodies, developed using 3,3'-diaminobenzidine chromogen, and counterstained with hematoxylin for nuclear visualization. Images were captured using a light microscope, and semi-quantitative analysis was performed.

2.8. Western blot analysis

Total protein was extracted from the control and TME groups using radioimmunoprecipitation assay lysis buffer supplemented with protease inhibitor cocktail and phosphatase inhibitors on ice. After centrifugation, the supernatants were collected, and protein concentrations were determined using a bicinchoninic acid protein assay kit (Cat. No. HY-K2002, MedChemExpress, Monmouth Junction, NJ, USA). Equal amounts of protein were mixed with loading buffer, denatured by boiling, separated by SDS–PAGE, and then transferred onto PVDF membranes. After blocking with 5% non-fat milk or 5% bovine serum albumin (BSA, Albumin, Bovine), Grade 625 (Cat. No. 4240GR250, Biofroxx, Einhausen, Germany) for 1 h at room temperature, the membranes were incubated overnight at 4 °C with primary antibodies against transforming growth factor-beta (TGF-β), phospho-nuclear factor-kappa B (p-NF-κB), and heat shock protein 90 (Hsp90). After washing, the membranes were incubated with the corresponding HRP-conjugated secondary antibodies for 1 h at room temperature. Protein bands were visualized using an enhanced chemiluminescence detection system, iBright FL1500 Imaging System (Thermo Fisher Scientific, Waltham, MA, USA). Hsp90 was used as the loading control.

2.9. Data presentation and statistical analysis

All quantitative data are presented as mean ± standard deviation or mean ± standard error of the mean. Statistical analyses were performed using GraphPad Prism 9.0 (USA) or R software (v4.2.0). For comparisons between two groups, an unpaired, two-tailed Student's *t*-test was used. For experiments involving more than two groups, one-way or two-way analysis of variance (ANOVA) was applied, followed by appropriate post-hoc tests.In this study, a p-value < 0.05 was considered statistically significant and is indicated with asterisks in the figures ($^*p < 0.05$, $^{**}p < 0.01$, $^{***}p < 0.001$, $^{****}p < 0.0001$).

3. Results

3.1. Fabrication and characterization of the biomimetic tumor microenvironment hydrogel

To precisely construct a biomimetic osteosarcoma microenvironment, this study developed a novel composite hydrogel-based bioink (designated as DHC hydrogel), primarily composed of dECM, CS, and HAP (Figure 1a,b). Previous studies have demonstrated that dECM hydrogels prepared through an optimized decellularization protocol exhibit favorable thermoresponsive gelation properties.[23]Type I collagen is the main component of dECM, and the preservation of key ECM components, including fibronectin, hyaluronic acid, and proteoglycans, helps maintain biological activity and mimic the soft bone marrow microenvironment.[24]

Chondroitin sulfate is capable of interacting with collagen fibers and proteoglycans in bone tissue, forming composite structures with favorable mechanical properties and biological functionality.[25] HAP is the primary inorganic component of human bone and teeth. Previous studies have shown that tumor cells interact with mineralized bone matrices within the osteosarcoma microenvironment.[25] Therefore, the incorporation of CS and HAP into the hydrogel system can effectively simulate the mineralization characteristics of bone, enhance the biocompatibility and mechanical properties of the hydrogel, and ultimately generate a more realistic biomimetic microenvironment.

Scanning electron microscopy analysis revealed that the prepared DHC hydrogel exhibited a highly porous and

loosely structured microarchitecture, with HAP particles uniformly dispersed on its surface (Figure 1c–e). Such a porous structure is critical for cell encapsulation, nutrient exchange, and the recapitulation of *in vivo*-like tissue microenvironments. Since SEM-based imaging may alter native pore morphology during sample dehydration, we further performed label-free reflectance confocal imaging of hydrated type I collagen hydrogels. Because the reflectance analysis was performed on hydrated type I collagen hydrogels rather than the full DHC formulation, these images should be interpreted as showing the hydrated fibrillar architecture of a collagen-rich surrogate matrix. Under fully hydrated conditions, the collagen matrix exhibited an interconnected fibrillar network with abundant interfibrillar voids, as visualized by single-plane and z-stack reflectance imaging (Figure S1a–c). These data complement the SEM results and more directly reflect the matrix architecture experienced by cells in the hydrated hydrogel environment.

A series of hydrogels fabricated by sequential addition of HAP/CS to dECM were characterized and demonstrated similar core properties, including favorable viscoelasticity, high water absorption, and slow degradation (Figure 1f–h). These characteristics are essential for maintaining long-term stability during *in vitro* culture.

In terms of mechanical properties, the effective Young's moduli of the four hydrogels ranged from 80 to 120 Pa (Figure 1k). Among the tested formulations, the DHC hydrogel exhibited the highest Young's modulus (~120 Pa; Figure 1k), with an effective Young's modulus of approximately 120 Pa—a value that is consistent with a soft marrow-like microenvironment. The material also displayed ideal shear-thinning behavior (Figure 1i) and was capable of undergoing a sol–gel phase transition under physiological temperature conditions (36 °C) (Figure 1j). Based on these comprehensive characteristics, the DHC hydrogel was ultimately selected as the optimal bioink for 3D bioprinting in this study. Subsequently, using a liquid–liquid printing approach, we employed the DHC hydrogel both as the bioink and as the supporting matrix to achieve planar and suspended printing of complex geometric patterns, thereby confirming its excellent printability (Figure 1l,m).

3.2. Biocompatibility assessment of composite hydrogels

To comprehensively evaluate the biocompatibility of the developed hydrogel materials, U2OS-RFP osteosarcoma cells, HMSCs, and 3D-bioprinted HUVECs (HUVEC-RFP) were cultured in different hydrogel matrices (Figure 2a). CLSM observations showed that, after 14 days of culture (Figure 2b), U2OS-RFP cells exhibited active proliferation and maintained normal morphology in all four hydrogel formulations (Figure 2c), indicating that these materials provided a permissive environment for osteosarcoma cell growth. In parallel, live/dead staining of HMSCs cultured for 14 days demonstrated that cell viability exceeded 90% in all groups (Figure 2d,f). Notably, HMSC proliferation was most pronounced in the DHC hydrogel compared with the other formulations (Figure 2e), further supporting that DHC provides a favorable stromal microenvironment.

To further characterize cell morphology within the 3D matrix, HMSCs and U2OS cells cultured in the DHC hydrogel for 3 days were stained with F-actin and DAPI (Figure 2g). Compared with conventional 2D culture, both cell types displayed more elongated, spindle-like morphologies and extended prominent cytoskeletal processes within the hydrogel, indicating active adaptation to the 3D environment. To better visualize the microstructural features of the engineered matrix, we further supplemented these observations with higher-resolution cytoskeletal imaging and two-photon microscopy. Confocal F-actin/DAPI staining revealed extensive cytoskeletal spreading and interconnected cellular organization within the construct (Figure S2a), while two-photon microscopy showed a close spatial association between the cellular network and the surrounding collagen matrix (Figure S2b). Together, these findings provide additional morphological evidence that the DHC-based microenvironment supports not only cell survival, but also structural integration between cells and the ECM.

In addition to supporting tumor and stromal cells, the DHC hydrogel also supported endothelial morphogenesis. HUVECs seeded into the DHC hydrogel via 3D bioprinting proliferated effectively and formed vessel-like sprouting structures over time (Figure 2i–k). The ability of HUVECs to generate vascular sprouts is an important indicator of angiogenic potential and suggests that the hydrogel can support the formation of a more physiologically relevant multicellular microenvironment.

Quantitative real-time polymerase chain reaction further highlighted the biological differences between 2D and 3D culture conditions (Figure 2h). Compared with 2D culture, 3D-cultured cells showed increased expression of *MMP9* in endothelial and tumor cells, whereas *MKI67* expression was decreased in HMSCs and tumor cells, consistent with a less proliferative but more invasion-associated state.[26,27] In addition, ECs showed increased expression of angiogenesis-related markers such as *CD34*, while tumor cells exhibited elevated *VEGFA* expression. These data suggest that the 3D hydrogel environment not only preserves viability, but also modulates cell state

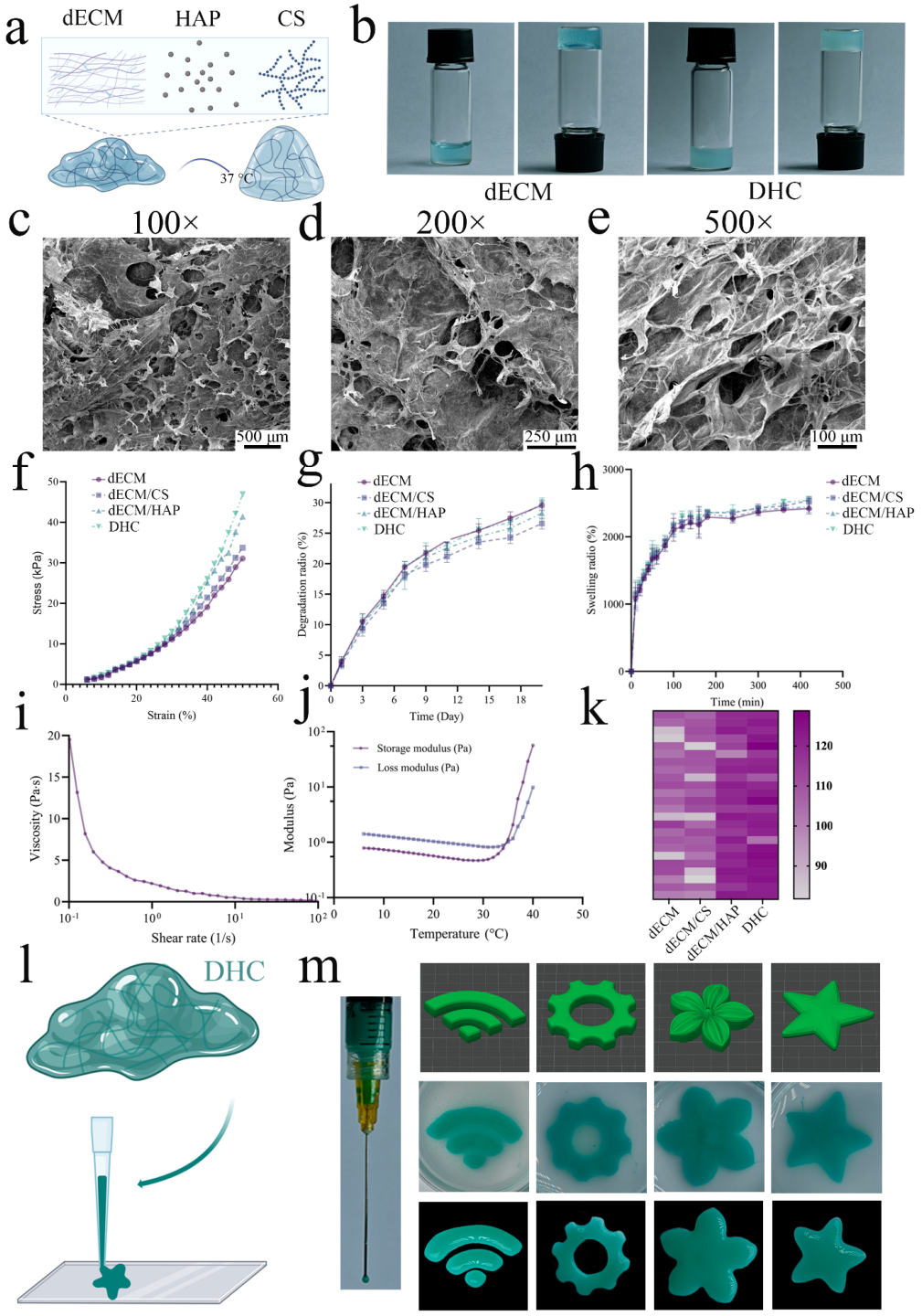

Figure 1. Fabrication of biomimetic mineralized hydrogel and bioink. (a) Schematic illustration of the preparation process for the DHC hydrogel. (b) Representative photographs of the DHC hydrogel before and after gelation. (c–e) SEM images of freeze-dried DHC hydrogel at magnifications of 100×, 200×, and 500×, respectively (scale bars: 500 μm, 250 μm, and 100 μm). (f) Compressive stress-strain curves of four different hydrogels. (g) Degradation profiles of the four hydrogels over a period of 20 days. (h) Swelling behavior of the four hydrogels. (i) Viscosity and shear stress distribution curves of the DHC hydrogel across a shear rate range from 1×10^{-1} to 1×10^{2} s^{-1}. (j) Thermogelation curve of the DHC hydrogel under a temperature gradient ranging from 4 °C to 40 °C. (k) Heatmap representation of the effective Young's moduli of the four hydrogels. (l) Schematic diagram illustrating the 3D bioprinting process. (m) Representative images of simple geometric models fabricated via 3D printing using the DHC hydrogel.
Abbreviations: CS: Chondroitin sulfate; dECM: decellularized extracellular matrix; HAP: Hydroxyapatite; SEM: Scanning electron microscopy.

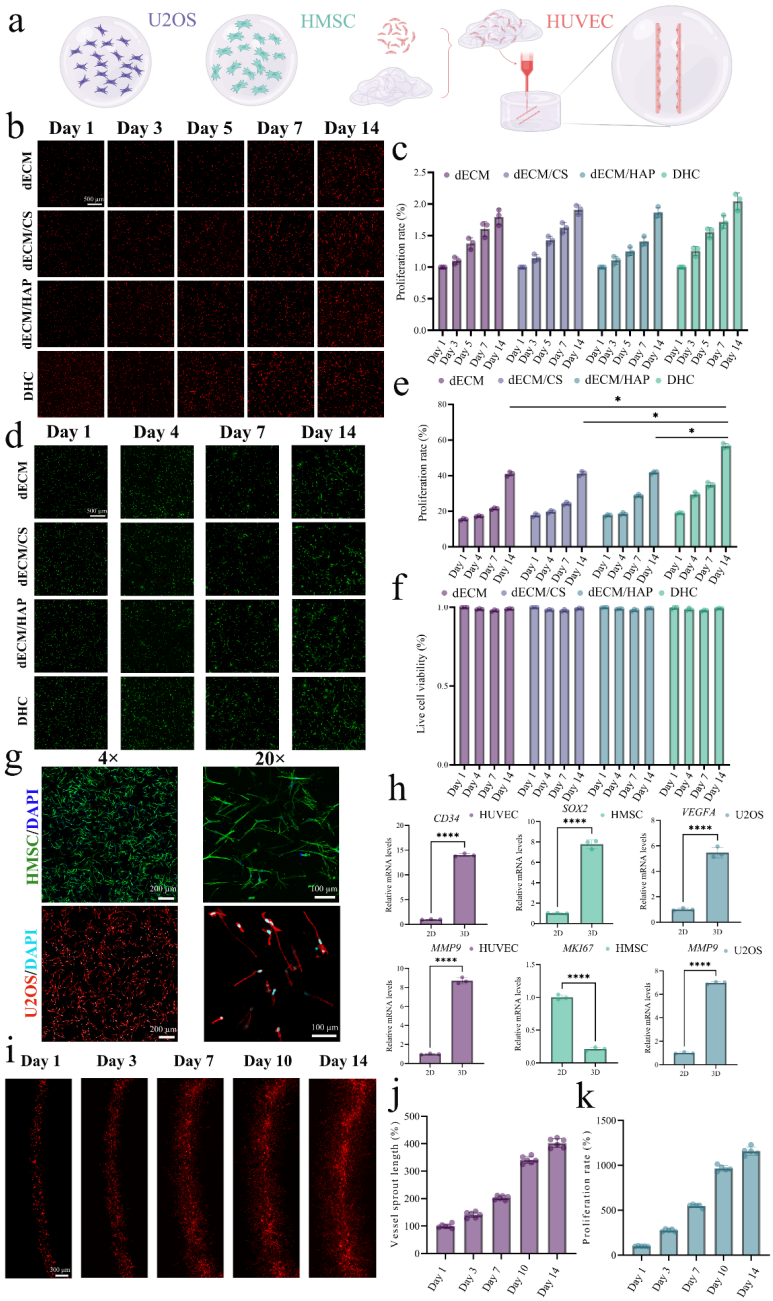

Figure 2. The DHC bioink and hydrogel provide a favorable microenvironment for cell growth. (a) Schematic illustration of cell culture in different hydrogels and vascular printing using the DHC bioink. (b) Representative fluorescence images showing U2OS-mCherry cells cultured within the four hydrogels. X–Y planar projections at days 1, 3, 5, 7, and 14 are presented. Scale bars: 500 μm; magnification: 4×. (c) Proliferation profiles of U2OS-mCherry cells in the four hydrogels. (d) Live/dead staining of HMSC-GFP cells cultured in the four hydrogels. Representative X–Y planar projections at days 1, 4, 7, and 14 are shown. Scale bars: 500 μm; magnification: 4×. (e) Proliferation dynamics of HMSC-GFP cells in the four hydrogels. (f) Viability ratios of HMSC-GFP cells in the four hydrogels. (g) F-actin and DAPI staining images of HMSCs and U2OS cells cultured in the DHC hydrogel for 3 days. Scale bars: 200 μm/100 μm; magnification: 4×/20×. (h) Gene expression profiles of U2OS cells, HMSCs, and HUVECs under 2D and 3D culture conditions. (i) Representative fluorescence images showing vascular structures formed by printed HUVEC-mCherry cells in the DHC hydrogel. X–Y planar projections at days 1, 3, 7, 10, and 14 are displayed. Scale bars: 300 μm; magnification: 4×. (j) Average sprout length of HUVEC-mCherry cells over time. (k) Proliferation profiles of HUVEC-mCherry cells in the DHC hydrogel. Statistical analysis was performed using one-way ANOVA and paired *t*-tests ($n = 3$). Significance levels are indicated as: ns (not significant), $^{*}p < 0.05$, $^{**}p < 0.01$, $^{***}p < 0.001$, $^{****}p < 0.0001$.

Abbreviations: CS: Chondroitin sulfate; dECM: decellularized extracellular matrix; HAP: Hydroxyapatite; HMSC: Human mesenchymal stem cell; HUVEC: Human umbilical vein endothelial cell

and function in ways that are more consistent with a physiologically relevant microenvironment.

Taken together, these results demonstrate that the DHC bioink provides a supportive environment for the survival, growth, and structural organization of tumor, stromal, and ECs. Compared with conventional 2D culture, the 3D hydrogel system promoted more physiologically relevant morphology, closer cell–matrix interaction, endothelial sprouting, and distinct transcriptional changes associated with invasion and angiogenesis, supporting its use as a biomimetic platform for subsequent osteosarcoma microenvironment modeling.

3.3. Construction of a 3D-bioprinted osteosarcoma microenvironment model and cell interactions

After confirming the biocompatibility of the hydrogels, this study successfully fabricated tumor spheroids with 3D structures using 3D bioprinting technology, laying the groundwork for constructing a biomimetic osteosarcoma microenvironment (Figure 3a). We utilized a bioink mixture containing U2OS and HMSC cells to successfully print biomimetic TME spheroids with a diameter of 1 mm. F-actin and DAPI staining confirmed that these spheroids exhibited healthy growth characteristics (Figure 3b). After 7 days of culture, the peripheral regions of the tumor spheroids showed higher cell density, with elongated and larger spindle-shaped morphology indicative of invasive growth into the surrounding matrix. In contrast, the central region of the spheroids had significantly fewer cells, likely due to oxygen and nutrient limitations. These findings are consistent with previous spheroid-based studies, showing that peripheral tumor-cell growth is more rapid than the growth in the central region.[28]

To enable continuous observation of the biological behavior of 3D tumor spheroids, we further printed tumor spheroids incorporating fluorescently labeled U2OS-RFP and HMSC-GFP cells (Figure 3c). Compared to tumor spheroids printed solely with U2OS-RFP cells, those co-cultured with HMSCs exhibited a reduced proliferation rate (Figure 3d). This reduced proliferation may reflect complex interactions between HMSCs and U2OS tumor cells. Under certain conditions, HMSCs can exert anti-proliferative effects on osteosarcoma cells, for example, by secreting cytokines or miRNAs (such as let-7f) contained in extracellular vesicles, which can inhibit tumor cell proliferation. On day 7 of culture, we performed FACS to isolate U2OS tumor cells from the microenvironment group and conducted cell cycle analysis in comparison with U2OS cells from the control group (Figure 3f). These results further supported this observation, showing a significantly higher proportion of tumor cells arrested in the G0–G1 phase in the experimental group, consistent with reduced proliferation.Notably, although proliferation was suppressed, the experimental group exhibited more pronounced spheroid expansion (Figure 3e), suggesting that the migratory and invasive capacity of tumor cells may have been enhanced. This highlights the dual role of HMSCs within the TME—they not only influence tumor cell behavior through ECM remodeling, but may also promote tumor cell migration and invasion by secreting chemokines or other signaling molecules.

Subsequently, we employed a dual-nozzle bioprinting technique to simultaneously fabricate both a vascular network composed of HUVEC cells and tumor spheroids co-constructed by HMSCs and U2OS cells, successfully establishing a vascularized osteosarcoma microenvironment model *in vitro* (Figure 3g). After 3 days of culture, all three cell types exhibited clear structural organization and differentiation within the matrix, and notably, enhanced vascular sprouting toward the tumor regions was observed (Figure 3h). This phenomenon may be attributed to the secretion of angiogenic factors by both tumor cells and HMSCs, which promote HUVEC proliferation and sprouting.

On day 7 of culture, we successfully isolated HUVECs, HMSCs, and U2OS cells from the vascularized TME using FACS. RT-qPCR analysis of U2OS cells from the vascularized TME group revealed a moderate decrease in the expression of *MKI67* and *PCNA*, while the expression levels of *MMP9* and *VEGFA* were significantly upregulated compared to those in the group with tumor spheroids alone (Figure 3i). These results further support the interpretation that tumor cells within the osteosarcoma microenvironment exhibit enhanced invasion-associated and angiogenic features, while HMSCs may suppress tumor-cell proliferation.

To further investigate the impact of the microenvironment on tumor biology, we performed transcriptomic sequencing on each of the three cell types isolated via FACS. The control group consisted of cells that were individually bioprinted and cultured under identical conditions for seven days. The heatmap of DEGs in U2OS and HMSC cells clearly revealed substantial transcriptional differences between the microenvironment–co-cultured group and the standalone 3D-printed group (Figure 3j,k).

This apparent paradox of concomitant proliferation suppression and enhanced invasiveness suggests a profound rewiring of key signaling networks within the tumor cells. We hypothesize that signals originating from the TME, particularly from HMSCs, may fine-tune the activity of core pathways such as Ras-MAPK, leading to a "decoupling" of the proliferative and migratory functional

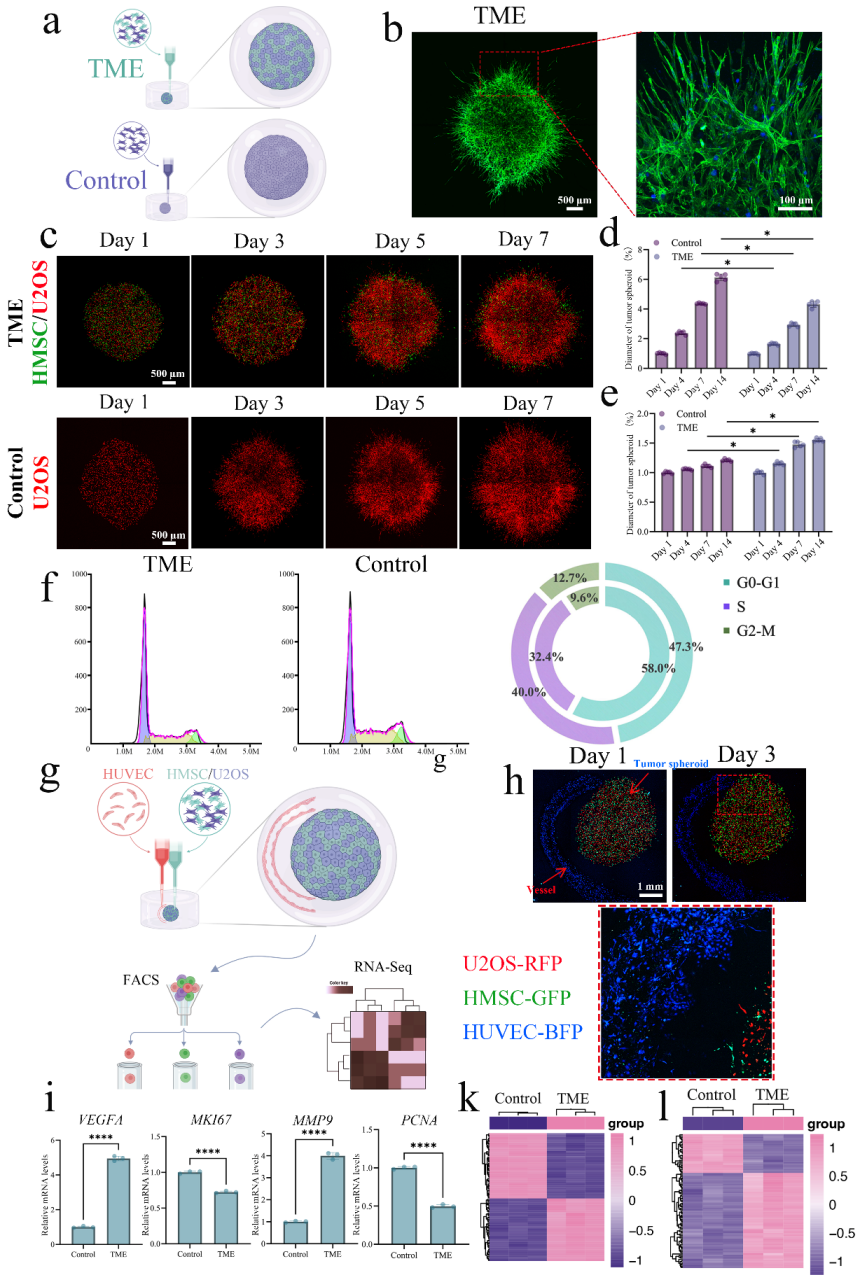

Figure 3. Construction of a vascularized osteosarcoma microenvironment model via 3D bioprinting. (a) Schematic illustration of the 3D bioprinting process using DHC bioink for both the control group and the TME group. (b) Representative F-actin and DAPI staining images showing cell morphology in the TME group on day 7. Scale bars: 500 μm/100 μm; magnification: 4×/20×. (c) Representative fluorescence images showing cell growth in the control group and the TME group at days 1, 3, 5, and 7. In these images, U2OS tumor cells are shown in red (mCherry), and HMSCs are shown in green (GFP). X–Y planar projections are presented. Scale bars: 500 μm; magnification: 4×. (d) Proliferation profiles of U2OS cells in the TME group versus the control group. (e) Comparative analysis of dynamic changes in the diameter of 3D-printed tumor structures between the TME group and the control group. (f) Flow cytometry-based cell cycle distribution profiles of U2OS cells from both groups. (g) Schematic diagram illustrating the construction of the vascularized TME model and subsequent transcriptomic analysis following FACS. (h) Representative fluorescence images of the vascularized TME model at days 1 and 3. In these images, U2OS tumor cells are shown in red, HMSCs are shown in green, and HUVECs are shown in blue. X–Y planar projections are displayed. Scale bars: 1 mm; magnification: 2.5×. (i) RT-qPCR analysis showing differential gene expression of U2OS cells between the control group and the TME group. (j) Heatmap of differentially expressed genes in U2OS cells. (k) Heatmap of differentially expressed genes in HMSCs. Statistical significance was determined by paired *t*-tests. Significance levels are indicated as: ns (not significant), $*p < 0.05$, $**p < 0.01$, $***p < 0.001$, $****p < 0.0001$. Abbreviations: CS: Chondroitin sulfate; dECM: decellularized extracellular matrix; FACS: Fluorescence-activated cell sorting; HAP: Hydroxyapatite; HMSC: Human mesenchymal stem cell; HUVEC: Human umbilical vein endothelial cell; TME: Tumor microenvironment.

modules.[29,30] Such regulation may allow downstream signals to drive cytoskeletal remodeling and cell motility, yet fail to reach the threshold required to initiate cell cycle progression in terms of either signal strength or duration. This phenomenon has been previously reported in other biological systems.[31,32]

3.4. Transcriptomic sequencing reveals the regulatory mechanisms of the tumor microenvironment and cell interactions through integration with single-cell sequencing databases

Further analysis of the transcriptomic sequencing data suggested broad changes in the functional state of tumor cells under vascularized TME conditions. GSEA results indicated that pathways related to the cell cycle, such as E2F Targets, MYC Targets V1, and G2M Checkpoint, were significantly downregulated in U2OS cells within the vascularized TME group (Figure 4a). This suggests that the presence of a vascularized TME, particularly HMSCs, can inhibit the proliferative activity of tumor cells. E2F and MYC are core transcription factors regulating cell cycle progression, and their reduced expression or activity directly leads to cell cycle arrest, consistent with our observed growth inhibition *in vitro*.

Concurrently, metabolic pathways were remodeled: OXPHOS, glycolysis, and cholesterol homeostasis pathways were all upregulated. This indicates that osteosarcoma cells maintain active glycolysis to support energy metabolism while also enhancing energy supply through mitochondrial oxidative phosphorylation when situated within a complex microenvironment. Notably, GSEA also revealed the promoting effects of the vascularized TME on tumor cells, including activation of epithelial–mesenchymal transition (EMT), hypoxia response, angiogenesis, and TGF-β signaling pathways. These findings suggest that, despite reduced proliferation, tumor cells under TME conditions acquire transcriptional features associated with invasion, hypoxia adaptation, and angiogenesis.

To further explore the multicellular interaction mechanisms within the TME, we performed KEGG pathway enrichment analysis on the three co-cultured cell types. The results showed that key signaling pathways such as Ras, Rap1, phospholipase D, NOTCH, NF-κB, MAPK, JAK-STAT, HIF-1, cAMP, and calcium signaling were coordinately upregulated across all three cell types (Figure 4b). To further support the transcriptomic findings at the protein level, we performed Western blot analysis for TGF-β and p-NF-κB in the control and TME groups. Both proteins showed higher expression in the TME group than in the control group, with comparable Hsp90 loading control signals, providing additional evidence that TGF-β-associated and NF-κB-associated signaling are enhanced under TME conditions (Figure S3). This suggests that the vascularized TME is accompanied by coordinated signaling changes across multiple cell types, consistent with enhanced multicellular interactions. Previous studies have shown that the Ras/MAPK and JAK-STAT pathways act as cores driving continuous tumor cell proliferation, while the NF-κB pathway ensures their survival by inhibiting apoptosis.[33–35] To meet growth demands, the HIF-1 and NOTCH pathways are activated to promote angiogenesis. Additionally, NOTCH, NF-κB, phospholipase D, and calcium signaling pathways confer potent invasive and migratory capabilities to cancer cells, which are critical for distant metastasis. The complex network involving pathways such as cAMP and Rap1 collectively regulates the dynamic interactions among cells in the TME, ultimately facilitating the invasion and malignant phenotype of osteosarcoma.

Further analysis of ligand–receptor interactions using the iTALK tool revealed that, compared to the control group, the vascularized TME exhibited a significantly increased number of communication events among U2OS, HUVEC, and HMSC, with a much higher network complexity (Figure 4d). This further corroborates at the molecular level that tight cell–cell interactions are central to the functional dynamics of the TME. HMSCs were found to highly express the chemokines CXCL5 and CXCL8, while U2OS cells expressed their corresponding receptor CXCR2, forming the CXCL/CXCR2 signaling axis. This axis has been widely reported to participate in pro-inflammatory and pro-angiogenic processes, suggesting that it may represent one of the key paracrine mechanisms by which HMSCs regulate tumor cell EMT and angiogenesis.[36–38]

To validate the clinical relevance of findings from our *in vitro* 3D model, we analyzed a publicly available scRNA-seq dataset (GSE152048)[39], which includes samples from six patients with primary osteosarcoma (Figure 4e). We successfully isolated populations of tumor cells, ECs, and MSCs from this dataset. Notably, tumor cells were further clustered into five distinct subpopulations based on the expression of proliferation-related genes, including one highly proliferative subgroup (OS_5) and four other subgroups.

By integrating bulk RNA-seq data of MSCs and ECs with the five tumor cell subpopulations identified in the single-cell transcriptome, we performed intercellular communication analysis (Figure 4f). The results revealed that the vascularized TME group exhibited significantly stronger communication between MSCs/ECs and all tumor subpopulations compared to the control

group. Importantly, this enhanced communication was predominantly observed between MSCs/ECs and the non-highly proliferative tumor subpopulations, whereas interactions with the highly proliferative OS_5 subgroup were relatively weaker.

AUCell pathway activity analysis further demonstrated (Figure 4g) that the OS_5 subgroup exhibited high activity of proliferation gene sets but low EMT activity, with a transcriptional profile closely resembling that of U2OS cells cultured in monoculture *in vitro*. In contrast, the other subgroups (OS_1–4) displayed low proliferation and high EMT features, consistent with those observed in the vascularized TME group.

Importantly, our model did not induce a general "invasive" phenotype, but rather selectively enriched for or induced a specific tumor cell population characterized by low proliferation and high EMT. This population showed a transcriptional signature highly similar to the unique tumor cell clusters (OS_1–4) identified in clinical osteosarcoma samples (Figure 4g). These findings indicate that our model successfully recapitulates a TME capable of nurturing a reservoir of quiescent, invasive "cancer stem-like" cells—widely recognized as the key drivers of tumor metastasis and post-treatment relapse.

3.5. *In vivo* effects of 3D-bioprinted tumor microenvironment on osteosarcoma progression

To investigate the *in vivo* effects of the *in vitro*-engineered 3D-bioprinted TME on osteosarcoma biology, we subcutaneously implanted the successfully constructed 3D-bioprinted osteosarcoma microenvironment models into nude mice. Given the low tumorigenicity of U2OS cells and the need for *in vivo* imaging, highly tumorigenic 143B-LUC cells expressing luciferase were used for the experiments.

Figure 5a illustrates the successful tumor formation and subsequent excision of the 3D-printed model in nude mice, along with the tissue processing workflow. During the 21-day observation period, there was no significant difference in body weight between the microenvironment group and the control group (Figure 5b), indicating that the implantation did not cause obvious systemic toxicity or adverse reactions. Bioluminescence imaging results showed weaker tumor proliferation in the microenvironment group compared to the control group (Figure 5f). These findings were consistent with direct measurements of tumor volume and mass (Figure 5c–e). Collectively, these data indicate that the 3D-bioprinted TME suppressed overall osteosarcoma growth *in vivo*.

To further elucidate the specific effects of the 3D-bioprinted TME on osteosarcoma biology, we performed histological sectioning and staining analyses on the excised tumors (Figure 5g). Masson's trichrome staining confirmed significantly increased collagen fiber deposition in the microenvironment group, forming a dense ECM. IHC staining for alpha-smooth muscle actin (α-SMA) revealed a notable enrichment of α-SMA-positive myofibroblasts in the tumor stroma of the microenvironment group. These enriched cancer-associated fibroblasts are crucial components of the TME known to promote tumor progression, invasion, and angiogenesis by remodeling the ECM and secreting cytokines. CD31 staining indicated a significant increase in microvessel density, suggesting enhanced angiogenic capacity. High expression of vimentin suggested that some tumor cells within the TME may have undergone EMT, exhibiting a potential trend toward increased invasiveness. Ki-67 immunohistochemistry, as a marker of cell proliferation, revealed that despite enhanced tumor invasion and angiogenesis, the Ki-67 positivity rate was significantly lower in the microenvironment group, indicating suppressed tumor cell proliferation.In summary, the *in vivo* animal experimental results align closely with our *in vitro* findings, collectively revealing the complex regulatory effects of the 3D-bioprinted TME on osteosarcoma biology. Specifically, the engineered TME suppressed overall tumor growth while being associated with angiogenesis, matrix remodeling, and invasion-related features.

3.6. Reduced chemosensitivity in the 3D-bioprinted osteosarcoma microenvironment

We further investigated the effect of the osteosarcoma TME on tumor cell chemosensitivity. Paclitaxel was initially used as a proof-of-concept chemotherapeutic agent, and CCK-8 assays showed that both 3D culture conditions and HMSC co-culture increased the IC_{50} value of U2OS cells relative to 2D culture (Figure 6a), suggesting reduced drug sensitivity under microenvironment-associated conditions.

To further validate this phenotype in the engineered TME model, tumor spheroids bioprinted from U2OS and HMSC cells were treated with 1 μM paclitaxel. On day 7, F-actin and DAPI staining revealed that cells in the control group exhibited more fragmented and condensed nuclei, whereas cells in the TME group retained relatively preserved morphology (Figure 6b). Live/dead staining further supported this difference (Figure 6c–f), showing that the TME group maintained a higher proportion of viable cells than the control group after treatment. In addition, dissociated tumor cells were analyzed by flow cytometry for live/dead status and apoptosis (Figure 6f–j). Compared with the control group, the TME group showed a higher proportion of viable tumor cells and a lower proportion of apoptotic cells following paclitaxel exposure. Together,

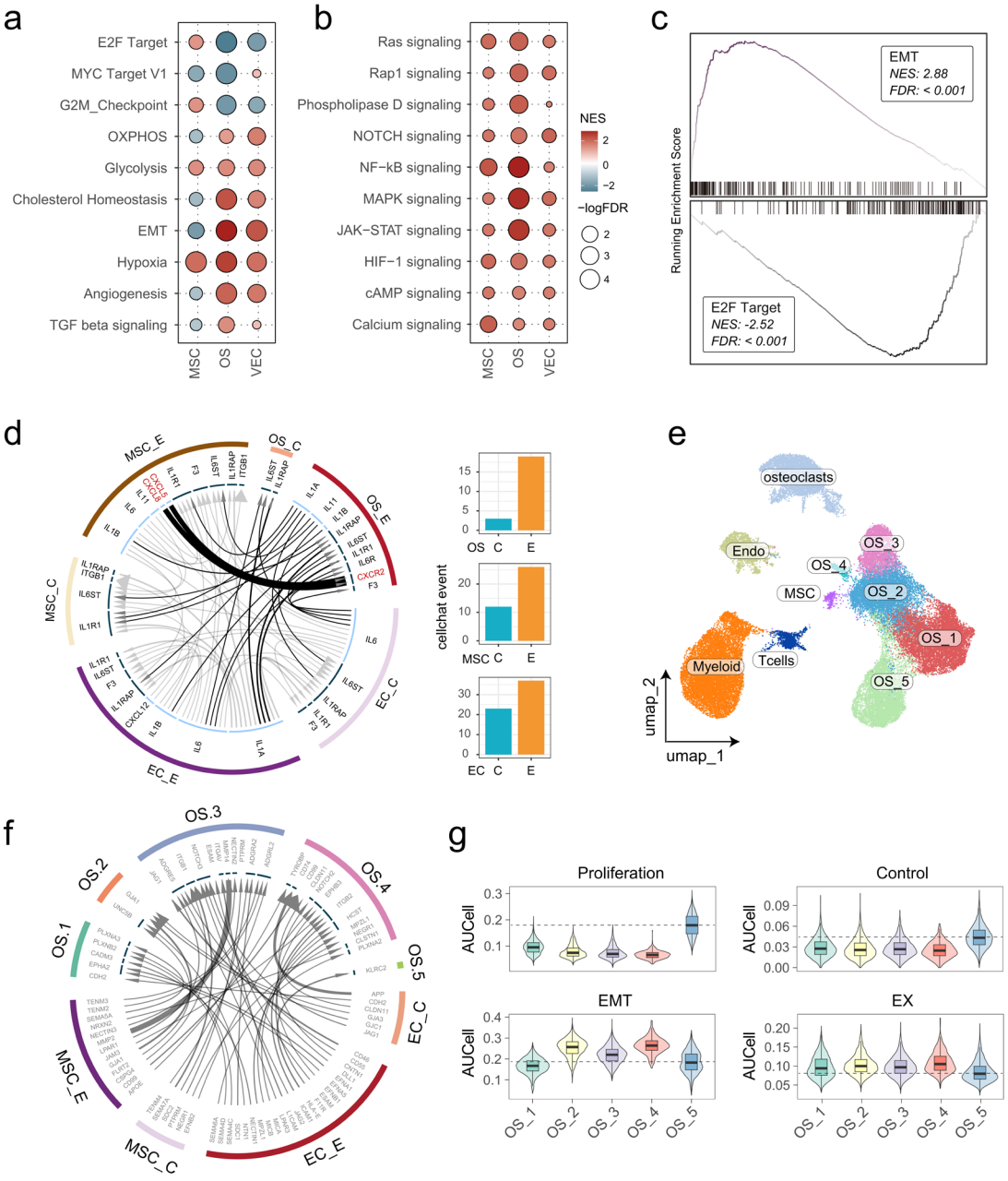

Figure 4. Transcriptomic analysis of the vascularized TME model. (a) GSEA enrichment analysis based on the Hallmark gene set reveals differentially activated pathways between the vascularized TME and the control group. (b) GSEA enrichment analysis based on KEGG pathways reveals distinct signaling pathways activated in the vascularized TME compared to the control group. (c) GSEA enrichment analysis of EMT and E2F Target pathways in U2OS cells. (d) Ligand–receptor interaction network among tumor cells, HMSCs, and HUVECs in the vascularized TME, constructed using the iTALK algorithm. (e) UMAP dimensionality reduction plot of single-cell transcriptomic data from six primary osteosarcoma patients, annotated by cell type. (f) Ligand–receptor interaction network among tumor cells, HMSCs, and ECs in clinical samples of primary osteosarcoma, reconstructed using the iTALK algorithm. (g) Pathway activity score analysis of different cell clusters in the single-cell transcriptomic dataset, performed using the AUCell method. Statistical significance was determined by paired *t*-tests. Significance levels are indicated as: ns (not significant), *$p < 0.05$, **$p < 0.01$, ***$p < 0.001$, ****$p < 0.0001$.

Abbreviations: EMT: Epithelial–mesenchymal transition; EX: Experiment group/TME group; FDR: False discovery rate; GSEA: Gene set enrichment analysis; HMSC: Human mesenchymal stem cell; HUVEC: Human umbilical vein endothelial cell; KEGG: Kyoto Encyclopedia of Genes and Genomes; MSC: Mesenchymal stem cell; NES: Normalized enrichment score; OS: Osteosarcoma; TME: Tumor microenvironment; UMAP: Uniform manifold approximation and projection; VEC: Vascular endothelial cell.

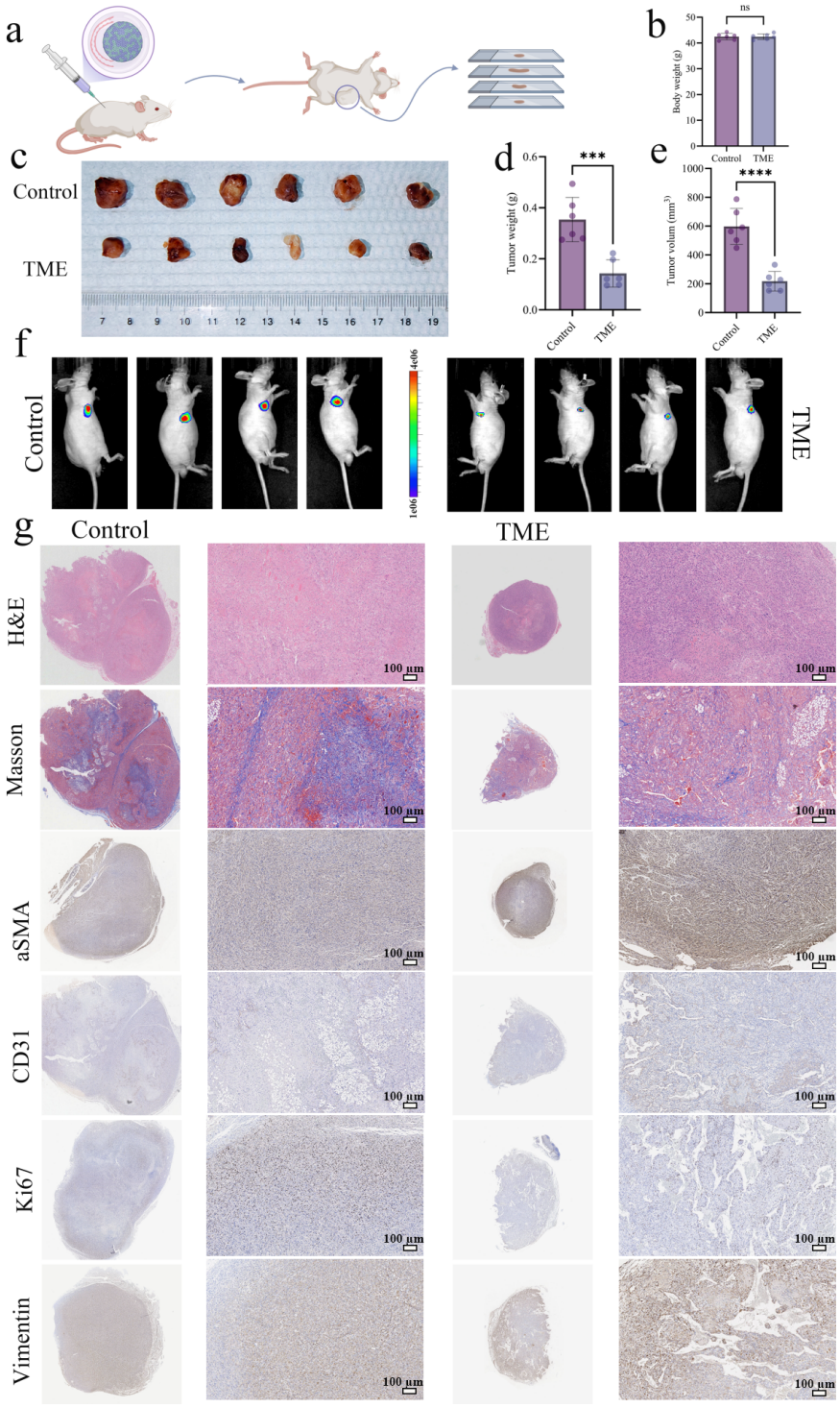

Figure 5. *In vivo* evaluation of the 3D-bioprinted tumor microenvironment in a murine model. (a) Schematic illustration of the mouse model construction. (b, d, e) Quantitative analysis of body weight (b), tumor weight (d), and tumor volume (e) in the two groups (n = 6). (c) Representative images of excised tumors from control and vascularized TME group mice on day 21. (f) *In vivo* bioluminescence imaging comparison between the control and vascularized TME groups on day 14. (g) Histological analysis of tumor tissues from both groups, including H&E staining, Masson's trichrome staining, and immunohistochemical staining for α-SMA, CD31, Ki-67, and vimentin. Scale bars: 100 μm; magnification: 20×. Statistical significance was determined by unpaired Student's t-test (n = 6). Significance levels are indicated as: ns (not significant), $^{*}p < 0.05$, $^{**}p < 0.01$, $^{***}p < 0.001$, $^{****}p < 0.0001$.
Abbreviations: α-SMA: Alpha-smooth muscle actin; H&E: Hematoxylin and eosin; TME: Tumor microenvironment.

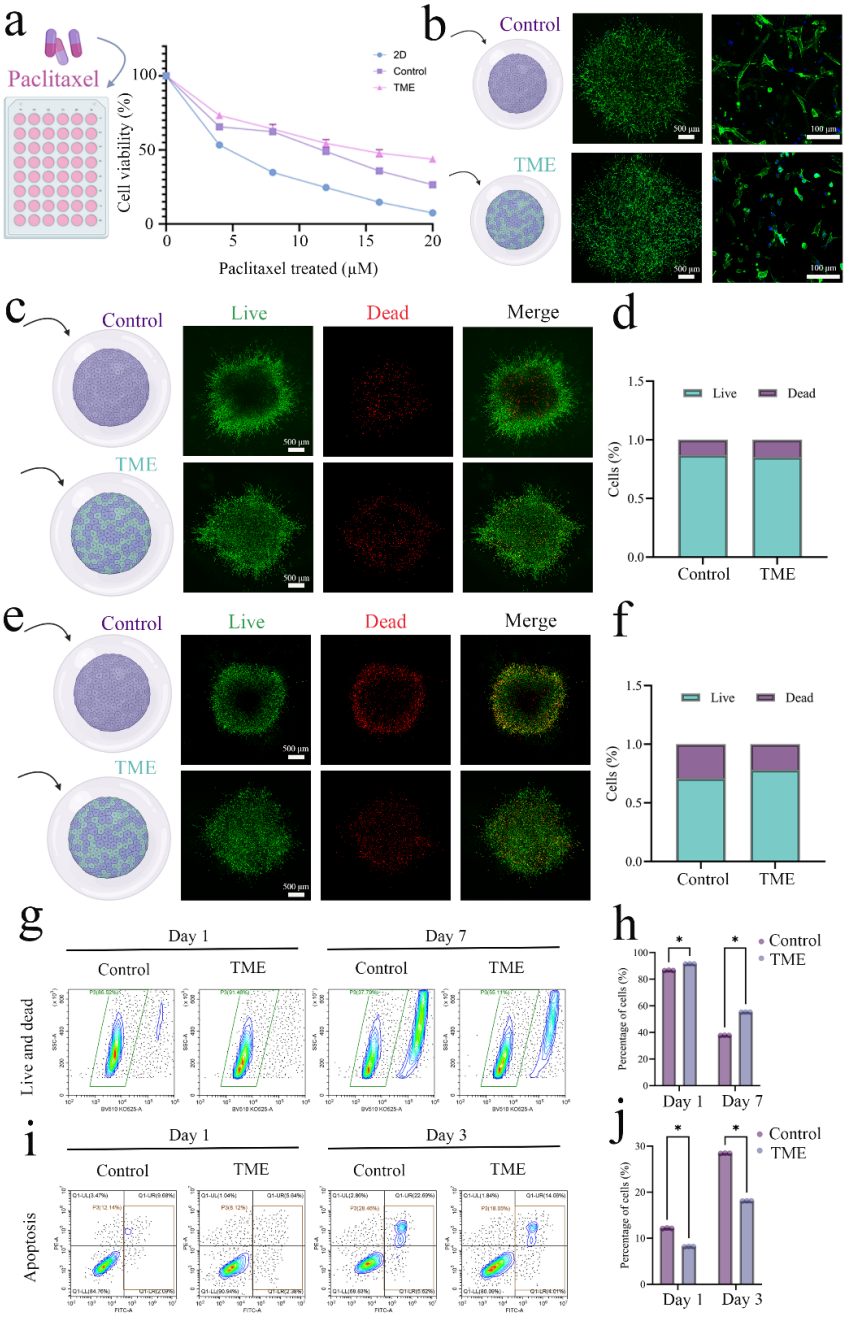

Figure 6. Chemosensitivity analysis of the 3D-bioprinted tumor microenvironment, including viability and apoptosis assessments. (a) Schematic illustration and results of the CCK-8 assay. (b) Schematic representation and representative F-actin/DAPI staining images showing morphological changes in cells after paclitaxel treatment in the control and TME groups. Scale bars: 500 μm/100 μm; magnification: 4×/20×. (c) Schematic diagram and representative fluorescence images showing cell viability status on day 3 after paclitaxel treatment in the control and TME groups. Scale bars: 500 μm; magnification: 4×. (d) Quantitative analysis of the live/dead ratio on day 3 after paclitaxel treatment. (e) Schematic diagram and representative fluorescence images showing cell viability status on day 7 after paclitaxel treatment in the control and TME groups. Scale bars: 500 μm; magnification: 4×. (f) Quantitative analysis of the live/dead ratio on day 7 after paclitaxel treatment. (g) Representative flow cytometry plots of live/dead staining in dissociated tumor cells from the control and TME groups. (h) Quantitative flow cytometric analysis of live/dead status in tumor cells on day 1 and day 7 after paclitaxel treatment. (i) Representative flow cytometry plots of apoptosis staining in dissociated tumor cells from the control and TME groups. (j) Quantitative flow cytometric analysis of apoptosis in tumor cells on day 1 and day 7 after paclitaxel treatment. Statistical significance was determined by paired t-tests. Significance levels are indicated as follows: ns, not significant; $^{*}p < 0.05$; $^{**}p < 0.01$; $^{***}p < 0.001$; $^{****}p < 0.0001$.
Abbreviations: α-SMA: Alpha-smooth muscle actin; H&E: Hematoxylin and eosin; TME: Tumor microenvironment.

these results support that the engineered osteosarcoma microenvironment is associated with reduced sensitivity to paclitaxel.

To improve the clinical relevance of this analysis, we further evaluated two standard first-line osteosarcoma chemotherapeutic agents, cisplatin and doxorubicin. Tumor spheroids were treated with 50 μM cisplatin or 10 μM doxorubicin, respectively. In both treatment settings, live/dead staining showed that the TME group retained a higher proportion of viable cells and fewer dead cells than the control group after drug exposure (Figures S4a,b and S5a,b). Consistently, flow cytometric analysis of Annexin V staining demonstrated that the percentage of apoptotic tumor cells was lower in the TME group than in the control group following either cisplatin or doxorubicin treatment (Figures S4c,d and S5c,d). These findings indicate that the protective effect of the engineered microenvironment is not restricted to paclitaxel but extends to clinically relevant first-line agents.

The reduced chemosensitivity observed in this model may be related to TME-induced phenotypic reprogramming. One plausible explanation is that the quiescence-like shift and reduced proliferative activity of tumor cells decrease their vulnerability to cytotoxic treatment. In addition, transcriptomic analysis, together with limited protein-level validation, suggested activation of survival-associated pathways, including TGF-β- and NF-κB-related signaling, which may further contribute to protection from drug-induced apoptosis. Therefore, our model supports the view that reduced chemosensitivity under TME conditions is not simply a passive barrier effect, but is also associated with biologically regulated changes in tumor cell state.

4. Discussion

4.1. A low-proliferative, invasion-associated, and drug-tolerant tumor state in the biomimetic osteosarcoma microenvironment

Osteosarcoma remains difficult to treat, particularly in metastatic or recurrent settings, in part because conventional experimental models fail to adequately recapitulate the multicellular interactions and matrix-derived cues of the TME.[40] In the present study, we established a vascularized 3D-bioprinted osteosarcoma model and found that TME conditions were associated with reduced tumor cell proliferation, G0/G1 phase arrest, increased expression of invasion-related markers, and reduced sensitivity to chemotherapy. Rather than simply enhancing tumor growth, the engineered microenvironment appeared to shift osteosarcoma cells toward a quiescence-like, invasion-associated phenotype. These findings support the concept that the TME functions not merely as a structural context, but as an active regulator of osteosarcoma cell state.[41]

This coexistence of reduced proliferation and enhanced invasive features is consistent with the concept of tumor phenotypic plasticity under microenvironmental stress.[42] Previous studies have shown that osteosarcoma cells, like many other malignant cells, can adopt alternative cellular states in response to stromal signals, matrix remodeling, hypoxia, and treatment pressure.[43] In our model, the DHC hydrogel provided not only a 3D scaffold, but also a biomimetic environment containing mineralized and matrix-associated cues that may influence tumor behavior. Consistent with this, high-resolution confocal and two-photon imaging further showed interconnected cellular organization and close spatial association between cells and the collagen network, while hydrated-state reflectance imaging supported that the collagen-based matrix retained an interconnected fibrillar architecture under physiologically relevant conditions. Accordingly, the present platform may offer a useful system for studying how vascular and stromal elements reshape osteosarcoma cell phenotypes in a controlled 3D setting.

4.2. Mechanistic implications and graded confidence in interpretation

Our data suggest that stromal and vascular components, particularly HMSCs, contribute importantly to the phenotypic changes observed in this model. Transcriptomic analyses indicated activation of signaling programs related to TGF-β signaling, EMT, hypoxia, and inflammatory or stress-associated pathways under TME conditions. Among these, TGF-β- and NF-κB-associated signaling received additional protein-level support in the revised study, strengthening the interpretation that these pathways may participate in the low-proliferative, invasion-associated, and drug-tolerant tumor state identified here.[44]

At the same time, several mechanistic inferences should be interpreted more cautiously. For example, ligand–receptor analysis implicated the CXCL/CXCR2 axis as a potential stromal–tumor communication pathway in this model.[45] Given the established association of this axis with osteosarcoma progression and metastasis in previous studies, this finding is biologically plausible. However, in the current study, this inference is based primarily on transcriptomic and bioinformatic analyses, and therefore its causal role remains to be established through dedicated protein-level and functional perturbation experiments.[46] Similarly, the enrichment of α-SMA-positive stromal features and increased collagen deposition *in vivo* raises the possibility that stromal cells may acquire cancer-associated

fibroblast-like characteristics within the TME[47], but this interpretation should also be regarded as provisional in the absence of lineage-tracing or more comprehensive stromal phenotyping.

In addition, transcriptomic changes in glycolysis- and oxidative phosphorylation-related pathways suggest substantial metabolic remodeling under TME conditions.[48] However, the directionality and functional consequences of these metabolic shifts remain unclear. Therefore, while the present data support the idea that the vascularized osteosarcoma microenvironment is accompanied by broad signaling and metabolic reprogramming, further targeted validation will be required to determine which pathways are functionally required for the phenotypic changes observed.

4.3. Reduced chemosensitivity in the engineered tumor microenvironment

An important finding of this study is that the engineered TME was associated with reduced chemosensitivity of osteosarcoma cells. In the revised study, this phenotype was observed not only with paclitaxel, but also with the clinically relevant first-line agents cisplatin and doxorubicin, for which the TME group consistently showed higher viability and lower apoptosis after treatment. These results strengthen the clinical relevance of the model and suggest that the protective effect of the TME is not limited to a single drug class, but may reflect a broader microenvironment-associated drug-tolerant state.[49]

Several mechanisms may contribute to this reduced chemosensitivity. First, the quiescence-like shift induced by the TME may reduce the susceptibility of tumor cells to cytotoxic agents that preferentially affect actively proliferating cells.[50] Second, survival-associated signaling pathways identified in the TME condition, including TGF-β- and NF-κB-related programs, may help suppress drug-induced apoptosis and enhance stress adaptation.[51] Consistent with this interpretation, tumor cells in the TME group exhibited reduced apoptosis after exposure not only to paclitaxel, but also to cisplatin and doxorubicin. Together, these observations support the broader view that chemoresistance in osteosarcoma may be dynamically shaped by the microenvironment rather than being determined solely by tumor-intrinsic genetic alterations.

From a translational perspective, these findings highlight the limitations of tumor-cell-only drug testing platforms. If drug tolerance is partly induced by stromal support, vascular cues, and matrix context, then preclinical models that omit these components may overestimate therapeutic efficacy.[52] In this regard, the present 3D-bioprinted system may provide a more informative platform for evaluating therapies designed not only to target tumor cells directly, but also to disrupt microenvironment-dependent survival and adaptation.

4.4. Clinical relevance, study limitations, and future directions

The translational value of this model is supported by its partial concordance with clinical transcriptomic data. Analysis of a public osteosarcoma single-cell RNA-seq dataset revealed tumor subpopulations with distinct transcriptional states in patient samples.[53] Notably, the tumor state induced in our 3D-TME model resembled a low-proliferative, EMT-high tumor subpopulation identified in the clinical dataset.[54] Although this similarity does not establish direct biological equivalence, it suggests that the model recapitulates features of a clinically relevant and potentially aggressive osteosarcoma cell state.

Several limitations of the present study should be acknowledged. First, although the present study included Western blot validation for selected pathways, much of the mechanistic interpretation remained transcriptomic and bioinformatic inference-based.[55] Second, the current model lacks immune components, which are likely to influence TGF-β, NF-κB, chemokine-associated signaling, and treatment response *in vivo*.[56] Third, the study relied mainly on established cell lines and therefore does not fully capture the genetic and phenotypic heterogeneity of patient tumors.[56] Fourth, the *in vivo* validation used a subcutaneous xenograft model, which is useful for assessing tumor-forming behavior and stromal remodeling, but cannot fully reproduce the native bone microenvironment or the full metastatic process of osteosarcoma.[57]

Nevertheless, this choice was deliberate in the context of the present study. Because the implanted construct was a pre-assembled, multicellular, humanized 3D-bioprinted osteosarcoma microenvironment containing a biomimetic matrix together with tumor, stromal, and ECs, subcutaneous implantation provided a relatively permissive *in vivo* setting for evaluating construct survival, vascular integration, and stromal remodeling while minimizing host bone-specific confounding effects.[58] By contrast, orthotopic implantation into the murine tibia or femur would introduce additional bone injury, inflammatory repair responses, and murine marrow-derived influences, which could reduce the interpretability of the specific engineered-microenvironment effects examined here.

Future work should therefore prioritize several directions. Functional validation of candidate signaling pathways, particularly those inferred from transcriptomic

analyses, will be necessary to strengthen mechanistic conclusions. Incorporation of immune components, such as macrophages or other myeloid populations, may help establish a more comprehensive osteosarcoma TME model.[59] In addition, the use of patient-derived cells or organoid-like tumor materials may improve the clinical relevance of the platform for precision drug testing.[60] Finally, development of orthotopic implantation strategies for the printed constructs would further enhance physiological relevance and may provide a stronger bridge between engineered *in vitro* systems and *in vivo* disease biology.[61]

5. Conclusion

In summary, we developed a vascularized 3D-bioprinted osteosarcoma microenvironment model that recapitulates key features of TME-associated tumor plasticity. Within this model, osteosarcoma cells adopted a low-proliferative, invasion-associated, and drug-tolerant state, accompanied by G0/G1 phase arrest, increased invasive features, and reduced sensitivity to multiple chemotherapeutic agents. Transcriptomic analysis, together with limited protein-level validation, suggested that TGF-β- and NF-κB-associated signaling may contribute to this phenotypic transition, while additional candidate stromal–tumor communication pathways, including CXCL/CXCR2, warrant further functional investigation.

The model also showed transcriptional similarity to a low-proliferative, EMT-high tumor subpopulation identified in clinical osteosarcoma samples, supporting its biological relevance. At the same time, the current system does not yet incorporate immune components and was validated in a subcutaneous rather than orthotopic *in vivo* setting. Future studies integrating functional pathway validation, immune elements, patient-derived tumor materials, and orthotopic implantation will be important for further improving the translational utility of this platform. Overall, this study provides a useful experimental framework for investigating osteosarcoma microenvironmental biology and for testing therapeutic strategies aimed at overcoming TME-associated drug tolerance.

Acknowledgments

None.

Funding

This work was supported by the Natural Science Foundation of Guangdong Province (Grant No. 2021A1515010447 to Wei Guo).

Conflict of interest

The authors declare that they have no known competing financial interests or personal relationships that could have appeared to influence the work reported in this paper.

Author contributions

Conceptualization: Shuai Huang, Wei Guo
Data curation: Guang Tang, Ying Zhao
Formal analysis: Guang Tang, Zhongte Peng
Funding acquisition: Wei Guo
Investigation: Guang Tang, Zhongte Peng, Ying Zhao
Methodology: Guang Tang, Zhongte Peng, Ying Zhao
Project administration: Wei Guo
Resources: Guangfu Chen, Wei Guo
Software: Zhongte Peng, Xin Chen
Supervision: Shuai Huang, Guangfu Chen, Wei Guo
Validation: Ying Zhao, Xin Chen
Visualization: Guang Tang, Zhongte Peng
Writing–original draft: Guang Tang, Zhongte Peng
Writing–review & editing: Shuai Huang, Guangfu Chen, Wei Guo

Ethics approval and consent to participate

The animal study was reviewed and approved by the Institutional Animal Care and Use Committee (IACUC) at Guangzhou Huace Detection Co., Ltd. (Approval No. 202502002). The study used publicly available data sets (GSE152048) and commercial cell lines; therefore, specific ethics approval for human participation was not required.

Consent for publication

Not applicable.

Availability of data

The single-cell RNA sequencing data analyzed in this study are publicly available in the Gene Expression Omnibus database under accession number GSE152048. The other datasets generated during the current study are available from the corresponding author on reasonable request.

References

1. Mirabello L, Troisi RJ, Savage SA. Osteosarcoma incidence and survival rates from 1973 to 2004: data from the Surveillance, Epidemiology, and End Results Program. *Cancer*. 2009;115(7):1531–43.

   doi: 10.1002/cncr.24121

2. Xu G, Wu H, Zhang Y, *et al*. Risk and Prognostic Factors for Different Organ Metastasis in Primary Osteosarcoma: A Large Population-Based Analysis. *Orthop Surg*. 2022;14(4):714–719.

doi: 10.1111/os.13243

3. Zou Y, Kang J, Zhu S, *et al*. The osteosarcoma immune microenvironment in progression: PLEK as a prognostic biomarker and therapeutic target. *Front Immunol*. 2025;16:1651858.

   doi: 10.3389/fimmu.2025.1651858

4. Rodrigues J, Sarmento B, Pereira CL. Osteosarcoma tumor microenvironment: the key for the successful development of biologically relevant 3D in vitro models. *Vitro Model*. 2022;1(1):5–27.

   doi: 10.1007/s44164-022-00008-x

5. Zhu Y, Chen J, Chen C, *et al*. Deciphering mechanical cues in the microenvironment: from non-malignant settings to tumor progression. *Biomark Res*. 2025;13(1):11.

   doi: 10.1186/s40364-025-00727-9

6. Biray Avci C, Goker Bagca B, Nikanfar M, Takanlou LS, Takanlou MS, Nourazarian A. Tumor microenvironment and cancer metastasis: molecular mechanisms and therapeutic implications. *Front Pharmacol*. 2024;15:1442888.

   doi: 10.3389/fphar.2024.1442888

7. Mak IW, Evaniew N, Ghert M. Lost in translation: animal models and clinical trials in cancer treatment. *Am J Transl Res*. 2014;6(2):114–8.

8. Andreu-Sanz D, Gregor L, Carlini E, Scarcella D, Marr C, Kobold S. Predictive value of preclinical models for CAR-T cell therapy clinical trials: a systematic review and meta-analysis. *J ImmunoTherapy Cancer*. 2025;13(6):e011698.

   doi: 10.1136/jitc-2025-011698

9. Munoz-Garcia J, Jubelin C, Loussouarn A, *et al*. In vitro three-dimensional cell cultures for bone sarcomas. *J Bone Oncol*. 2021;30:100379.

   doi: 10.1016/j.jbo.2021.100379

10. Sandhu V, Bakkalci D, Wei S, Cheema U. Enhanced Biomimetics of Three-Dimensional Osteosarcoma Models: A Scoping Review. *Cancers*. 2023;16(1):164.

    doi: 10.3390/cancers16010164

11. Kortam S, Lu Z, Zreiqat H. Recent advances in drug delivery systems for osteosarcoma therapy and bone regeneration. *Commun Mater*. 2024;5(1):168.

    doi: 10.1038/s43246-024-00612-2

12. Mandeda Madaiah P, Ghosh RN, Namboothiri PK, Peter M. Advancement in Scaffold-Based 3D Cell Culture Models for Osteosarcoma Drug Screening. *ACS Biomater Sci Eng*. 2025;11(11):6426–6442.

    doi: 10.1021/acsbiomaterials.5c01174

13. Yu L, Zhang J, Li Y. Effects of microenvironment in osteosarcoma on chemoresistance and the promise of immunotherapy as an osteosarcoma therapeutic modality. *Front Immunol*. 2022;13:871076.

    doi: 10.3389/fimmu.2022.871076

14. Tu B, Zhu J, Liu S, *et al*. Mesenchymal stem cells promote osteosarcoma cell survival and drug resistance through activation of STAT3. *Oncotarget*. 2016;7(30):48296–48308.

    doi: 10.18632/oncotarget.10219

15. Zhou B, Sun M, Yang M, Cui W, Yang H. Construction and application of multicellular tumor microenvironment models based on three-dimensional bioprinting technology. *Hepatobiliary Surg Nutr*. 2025;14(4):692–696.

    doi: 10.21037/hbsn-2025-504

16. Son J, Li S, Jeong W. Bioprinting Vascularized Constructs for Clinical Relevance: Engineering Hydrogel Systems for Biological Maturity. *Gels*. 2025;11(8):636.

    doi: 10.3390/gels11080636

17. Du S, Yang J, Li H, Men S, Xu D, Wang H. Three-dimensional culture of tumor cells (Review). *Oncol Lett*. 2026;31(3):110.

    doi: 10.3892/ol.2026.15464

18. Domingues MF, Carreira MC, Santos MS, *et al*. A 3D Bioprinted Spheroid-Laden dECM-Enriched Osteosarcoma Model for Enhanced Drug Testing and Therapeutic Discovery. *Adv Healthc Mater*. 2026:e03633.

    doi: 10.1002/adhm.202503633

19. Tharakan S, Raja I, Pietraru A, *et al*. The Use of Hydrogels for the Treatment of Bone Osteosarcoma via Localized Drug-Delivery and Tissue Regeneration: A Narrative Review. *Gels*. 2023;9(4):274.

    doi: 10.3390/gels9040274

20. Leonteva A, Kazakova A, Berezutskaya E, *et al*. Heterotypic 3D Model of Breast Cancer Based on Tumor, Stromal and Endothelial Cells: Cytokines Interaction in the Tumor Microenvironment. *Cells*. 2026;15(2):145.

    doi: 10.3390/cells15020145

21. Cristini N, Tavakoli M, Sanati M, Yavari SA. Exploring bone-tumor interactions through 3D in vitro models: Implications for primary and metastatic cancers. *J Bone Oncol*. 2025;53:100698.

    doi: 10.1016/j.jbo.2025.100698

22. Chen J, Yang H. Convergent bioprinting and microfluidics: toward next-generation biomimetic tumor models. *Hepatobiliary Surg Nutr*. 2026;15(1):18.

    doi: 10.21037/hbsn-2026-1-0021

23. Barajaa MA, Otsuka T, Ghosh D, Kan H-M, Laurencin CT. Development of porcine skeletal muscle extracellular matrix–derived hydrogels with improved properties and low immunogenicity. *Proc Natl Acad Sci USA* 2024;121(19):e2322822121.

    doi: 10.1073/pnas.2322822121

24. Li C, An N, Song Q, *et al*. Enhancing organoid culture: harnessing the potential of decellularized extracellular matrix hydrogels for mimicking microenvironments. *J Biomed Sci*. 27 2024;31(1):96.

    doi: 10.1186/s12929-024-01086-7

25. Klara J, Marczak A, Łatkiewicz A, Horak W, Lewandowska-Łańcucka J. Lysine-functionalized chondroitin sulfate improves the biological properties of collagen/chitosan-based injectable hydrogels. *Int J Biol Macromol*. 2022;202:318–331.

    doi: 10.1016/j.ijbiomac.2022.01.026

26. Fontana F, Marzagalli M, Sommariva M, Gagliano N, Limonta P. In Vitro 3D Cultures to Model the Tumor Microenvironment. *Cancers*. 2021;13(12):2970.

    doi: 10.3390/cancers13122970

27. Loessner D, Stok KS, Lutolf MP, Hutmacher DW, Clements JA, Rizzi SC. Bioengineered 3D platform to explore cell–ECM interactions and drug resistance of epithelial ovarian cancer cells. *Biomaterials*. 2010;31(32):8494–8506.

    doi: 10.1016/j.biomaterials.2010.07.064

28. Friedrich J, Ebner R, Kunz-Schughart LA. Experimental anti-tumor therapy in 3-D: spheroids--old hat or new challenge? *Int J Radiat Biol*. 2007;83(11-12):849–871.

    doi: 10.1080/09553000701727531

29. Hendrikse CSE, Theelen PMM, van der Ploeg P, *et al*. The potential of RAS/RAF/MEK/ERK (MAPK) signaling pathway inhibitors in ovarian cancer: A systematic review and meta-analysis. *Gynecol Oncol*. 2023;171:83–94.

    doi: 10.1016/j.ygyno.2023.01.038

30. Sahai E, Olson MF, Marshall CJ. Cross-talk between Ras and Rho signalling pathways in transformation favours proliferation and increased motility. *Embo J*. 2001;20(4):755–766.

    doi: 10.1093/emboj/20.4.755

31. Witze ES, Litman ES, Argast GM, Moon RT, Ahn NG. Wnt5a control of cell polarity and directional movement by polarized redistribution of adhesion receptors. *Science*. 2008;320(5874):365–369.

    doi: 10.1126/science.1151250

32. Weeraratna AT, Jiang Y, Hostetter G, *et al*. Wnt5a signaling directly affects cell motility and invasion of metastatic melanoma. *Cancer Cell*. 2002;1(3):279–288.

    doi: 10.1016/s1535-6108(02)00045-4

33. Bahar ME, Kim HJ, Kim DR. Targeting the RAS/RAF/MAPK pathway for cancer therapy: from mechanism to clinical studies. *Signal Transduct Target Ther*. 2023;8(1):455.

    doi: 10.1038/s41392-023-01705-z

34. Braicu C, Buse M, Busuioc C, *et al*. A Comprehensive Review on MAPK: A Promising Therapeutic Target in Cancer. *Cancers*. 2019;11(10):1618.

    doi: 10.3390/cancers11101618

35. Zhang T, Ma C, Zhang Z, Zhang H, Hu H. NF-κB signaling in inflammation and cancer. *MedComm*. 2021;2(4):618–653.

    doi: 10.1002/mco2.104

36. Zhang W, Wang H, Sun M, *et al*. CXCL5/CXCR2 axis in tumor microenvironment as potential diagnostic biomarker and therapeutic target. *Cancer Commun*. 2020;40(2-3):69–80.

    doi: 10.1002/cac2.12010

37. Han ZJ, Li YB, Yang LX, Cheng HJ, Liu X, Chen H. Roles of the CXCL8-CXCR1/2 Axis in the Tumor Microenvironment and Immunotherapy. *Molecules*. 2021;27(1):137.

    doi: 10.3390/molecules27010137

38. Miyake M, Goodison S, Urquidi V, Gomes Giacoia E, Rosser CJ. Expression of CXCL1 in human endothelial cells induces angiogenesis through the CXCR2 receptor and the ERK1/2 and EGF pathways. *Lab Investig*. 2013;93(7):768–778.

    doi: 10.1038/labinvest.2013.71

39. Zhou Y, Yang D, Yang Q, *et al*. Single-cell RNA landscape of intratumoral heterogeneity and immunosuppressive microenvironment in advanced osteosarcoma. *Nat Commun*. 2020;11(1):6322.

    doi: 10.1038/s41467-020-20059-6

40. Odri GA, Tchicaya-Bouanga J, Yoon DJY, Modrowski D. Metastatic Progression of Osteosarcomas: A Review of Current Knowledge of Environmental versus Oncogenic Drivers. *Cancers*. 2022;14(2):360.

    doi: 10.3390/cancers14020360

41. Patrașcu AV, Țarcă E, Lozneanu L, *et al*. The Role of Epithelial-Mesenchymal Transition in Osteosarcoma Progression: From Biology to Therapy. *Diagnostics*. 2025;15(5):644.

    doi: 10.3390/diagnostics15050644

42. Syga S, Jain HP, Krellner M, Hatzikirou H, Deutsch A. Evolution of phenotypic plasticity leads to tumor heterogeneity with implications for therapy. *PLoS Comput Biol*. 2024;20(8):e1012003.

    doi: 10.1371/journal.pcbi.1012003

43. Böttger K, Hatzikirou H, Voss-Böhme A, Cavalcanti-Adam EA, Herrero MA, Deutsch A. An Emerging Allee Effect Is Critical for Tumor Initiation and Persistence. *PLoS Comput Biol*. 2015;11(9):e1004366.

    doi: 10.1371/journal.pcbi.1004366

44. Xue J, Yang XR, Wang L. NF-κB signaling pathway in osteosarcoma: from signaling networks to targeted therapy. *Front Oncol*. 2025;15:1565760.

    doi: 10.3389/fonc.2025.1565760

45. Liu G, An L, Zhang H, Du P, Sheng Y. Activation of CXCL6/CXCR1/2 Axis Promotes the Growth and Metastasis of Osteosarcoma Cells in vitro and in vivo. *Front Pharmacol*. 2019;10:307.

doi: 10.3389/fphar.2019.00307

46. Matsuoka T, Yashiro M. Bioinformatics Analysis and Validation of Potential Markers Associated with Prediction and Prognosis of Gastric Cancer. *Int J Mol Sci*. 2024;25(11):5880.

doi: 10.3390/ijms25115880

47. Hu J, Lazar AJ, Ingram D, *et al*. Cell membrane-anchored and tumor-targeted IL-12 T-cell therapy destroys cancer-associated fibroblasts and disrupts extracellular matrix in heterogenous osteosarcoma xenograft models. *J ImmunoTherapy Cancer*. 2024;12(1):e006991.

doi: 10.1136/jitc-2023-006991

48. Li X, Yang Y, Zhang B, *et al*. Lactate metabolism in human health and disease. *Signal Transduct Target Ther.* 2022;7(1):305.

doi: 10.1038/s41392-022-01151-3

49. Russo M, Chen M, Mariella E, *et al*. Cancer drug-tolerant persister cells: from biological questions to clinical opportunities. *Nat Rev Cancer*. 2024;24(10):694–717.

doi: 10.1038/s41568-024-00737-z

50. Wang L, Shang Z, Zhou Y, *et al*. Autophagy mediates glucose starvation-induced glioblastoma cell quiescence and chemoresistance through coordinating cell metabolism, cell cycle, and survival. *Cell Death Dis*. 2018;9(2):213.

doi: 10.1038/s41419-017-0242-x

51. Wang Y, Chen W, Wang Z, *et al*. Deciphering metabolic reprogramming of immune cells within the tumor microenvironment. *J Transl Med*. 2025;23(1):1055.

doi: 10.1186/s12967-025-07069-y

52. Rubahamya B, Dong S, Thurber GM. Clinical translation of antibody drug conjugate dosing in solid tumors from preclinical mouse data. *Sci Adv*. 2024;10(22):eadk1894.

doi: 10.1126/sciadv.adk1894

53. Lee H, Kim B, Park J, *et al*. Cancer stem cells: landscape, challenges and emerging therapeutic innovations. *Signal Transduct Target Ther*. 2025;10(1):248.

doi: 10.1038/s41392-025-02360-2

54. Ozmen F, Ozmen TY, Ors A, *et al*. Single-cell RNA sequencing reveals different cellular states in malignant cells and the tumor microenvironment in primary and metastatic ER-positive breast cancer. *npj Breast Cancer*. 2025;11(1):95.

doi: 10.1038/s41523-025-00808-w

55. Cao K, Shi Y, Wu B, *et al*. Single cell RNA sequencing decodes cellular heterogeneity and identifies prognostic immune signatures in bladder cancer microenvironment. *Discov Oncol*. 2025;16(1):2239.

doi: 10.1007/s12672-025-03878-1

56. Chuprin J, Buettner H, Seedhom MO, *et al*. Humanized mouse models for immuno-oncology research. *Nat Rev Clin Oncol*. 2023;20(3):192–206.

doi: 10.1038/s41571-022-00721-2

57. Zheng D. Orthotopic tumours, a hot topic for xenograft models? *eBioMedicine*. 2019;41:11–12.

doi: 10.1016/j.ebiom.2019.02.052

58. Nabel CS, Vander Heiden MG. Patient-Derived Xenografts to Study Cancer Metabolism: When Does X Mark the Spot? *Cancer Res*. 2021;81(17):4399–4401.

doi: 10.1158/0008-5472.Can-21-0770

59. Peng M, Zhu Y, Hu Y, Wen J, Huang W. Advances in the regulation of macrophage polarization by the tumor microenvironment. *Discov Oncol*. 2025;16(1):1487.

doi: 10.1007/s12672-025-03258-9

60. Picco G, Garnett MJ. A Road Map for Precision Cancer Medicine Using Personalized Models. *Cancer Discov*. 2017;7(5):456–458.

doi: 10.1158/2159-8290.CD-17-0268

61. Yousefieh N, Hahto SM, Stephens AL, Ciavarra RP. Regulated expression of CCL21 in the prostate tumor microenvironment inhibits tumor growth and metastasis in an orthotopic model of prostate cancer. *Cancer Microenviron*. 2009;2(1):59–67.

doi: 10.1007/s12307-009-0021-z